On the Source of Midlatitude Low-Frequency Variability. Part I: A Statistical Approach to Persistence

ROBERT VAUTARD* AND BERNARD LEGRAS

Laboratoire de Météorologie Dynamique, Ecole Normale Supérieure, Paris, France

MICHEL DÉQUÉ

C.N.R.M., Météorologie Nationale, Toulouse, France

(Manuscript received 27 July 1987, in final form 1 March 1988)

ABSTRACT

The forcing of low-frequency variability by synoptic transient traveling perturbations is investigated within a quasi-geostrophic channel forced by a localized baroclinic jet. Spontaneously generated baroclinic perturbations grow and decay along a storm track; at the end of the track a maximum of low-frequency variability is obtained, in agreement with atmospheric observations. The structure of low-frequency variability is studied with a combination of statistical methods, using a multivariate red noise model as a random reference. We show that the anomalies are preferentially linked with local stationary structures or long-wave vacillations according to their location and their sign.

A systematic study of persistence is conducted with a criterion based on rms of the streamfunction variations. The interesting quantity is the probability of persistence which shows a very inhomogeneous distribution in phase space and several separated maxima. The composites based on these maxima exhibit the characters of zonal and blocking regimes. The transient feedback has a positive role in extending the jet downstream but the primary effect is the maintenance of the blocking circulation.

1. Introduction

The existence of a complex coupling between low-frequency variability of the midlatitude circulation and synoptic activity is clearly established by a series of recent observations. A particularly puzzling problem is how transient eddies may sometimes maintain high amplitude large-scale anomalies as evidenced from various studies (e.g., Illari and Marshall 1983; Hoskins et al. 1983; Trenberth 1986; Mullen 1987; Holopainen and Fortelius 1987).

From the theoretical standpoint, it is shown by Egger and Schilling (1983) that the red-noise stochastic response of large scales to synoptic forcing accounts for a large part of the low-frequency variance, thus demonstrating that one cannot expect a simple linear statistical scheme to produce valuable extended large-scale forecast. But, this important result does not eliminate the possibility that extended predictability could be based on properties not captured by the simple analysis of spatial-temporal variance.

In a more dynamical framework, Simmons and Hoskins (1978) show that the nonlinear development of baroclinic instability induces a northward flux of potential vorticity at maturity. Shutts (1983) shows that a pure barotropic mechanism allows blocking dipoles to be maintained by traveling disturbances. In his study, an initial flow with a stationary dipole pattern is perturbed by a wave-maker located upstream from the dipole; disturbances are advected downstream and are split by the diffluence, then inducing a positive feedback on the dipole. In addition, blocks are spontaneously generated from pure nonlinear activity in another experiment with homogeneous initial conditions. These results suggest a generation mechanism of atmospheric blocking that does not involve any dynamical orographic effect. According to Hoskins et al. (1983), it can be sketched as follows: baroclinic disturbances generated in strong shear areas on eastern margins of the continents mature as they propagate downstream along storm tracks, develop a barotropic profile, and deposit their potential vorticity into large-scale barotropic dipoles at the exit of the storm tracks. Pierrehumbert (1984) provides an illuminative theoretical support for this scenario through the computation of the local unstable eigenmode of a basic diffluent jet

* Present affiliation: Department of Atmospheric Sciences, University of California; Los Angeles, CA 90024.

Corresponding author address: Dr. Bernard Legras, Laboratoire de Meteorologie Dynamique, Ecole Normale Supérieure, 24 rue Lhomond, 75231 Paris Cedex 05, France.

and of its feedback effect onto the mean flow. The main limitation of his approach is the lack of lateral degrees of freedom which hinders the development of nonlinearities (an essential element in Shutts' barotropic mechanism) and vacillations within the coupled system of synoptic waves and large-scale flow.

This article is the first part of a study aiming at the extension of the approach of Shutts towards consistency and realism, and at the development of suitable tools for the study of large-scale persistent anomalies. Unlike Shutts, we require the baroclinic perturbations to be generated by a localized shear jet (which simulates the atmospheric westerly jet) rather than being artificially introduced. To accomplish this goal, a minimal model possessing the desirable characters is designed. The first part of the study is devoted to a systematic analysis of the dynamical properties of our model by the combination of several complementary statistical methods. In the second part, we identify a series of weather regimes by using an objective definition of regimes, which is able to take into account the effect of transients.

As a general rule, our approach is based on the study of long integrations of our model rather than on the study of initial value problems. This is (within the framework of our model) to keep close to a practical observational standpoint and to make sure of only considering natural dynamical situations. In addition, none of the original methods presented in the two parts of this study are specific to the simplicity of the investigated model. Thus, the skill demonstrated herein shows their potential for the study of the general circulation of the atmosphere. Finally, we emphasize the importance of drawing a distinction between noise and coherent dynamics, that is of assessing what the features of atmospheric variability are that cannot be reproduced by the pure stochastic response studied by Egger and Schilling and thus require a specific dynamical explanation. It is natural to consider here the simplest conceivable stochastic model, a Markovian linear model, with the same variance and the same correlation at 1-day lag as our original model.

In section 2, we present our model and we define the basic flow and the set of parameters used in this study. Section 3 is devoted to the study of the linear behavior around the basic flow which illuminates some aspects of the dynamics diagnosed in the following sections. Section 4 presents the general features of the flow, showing how transients and stationary modes separate in both frequency and wavenumber domains. Section 4 also defines the multivariate red noise model which is used as a stochastic reference for persistence studies. In section 5, we study the persistence characteristics of the large scales and we produce composite maps for the configurations of highest probability of persistence. The sensitivity of the dynamics to variations of the prescribed parameters is discussed in section 6. Section 7 contains a summary and concluding remarks.

2. The model

The minimal set of equations in which we can investigate the coupling between low-frequency variability and traveling synoptic perturbations is the classic two-layer quasi-geostrophic model in a β-channel (Pedlosky 1979). Using the potential temperature $\theta = T(p_0/p)^\kappa$ as vertical coordinate, the potential vorticity is defined as

$$q = f_0 + \beta y + \Delta\psi - f_0^2\left(\frac{dp_s}{d\theta}\right)^{-1}\frac{p_0^\kappa}{\kappa C_p}\frac{\partial}{\partial\theta}\left(p_s^{1-\kappa}\frac{\partial\psi}{\partial\theta}\right), \quad (2.1)$$

where standard notations have been used. The time evolution of the potential vorticity is given by

$$\frac{\partial q}{\partial t} + J(\psi, q) = G + E, \quad (2.2)$$

where J is the Jacobian operator, E groups the dissipation terms, and G is a constant forcing.

Equation (2.2) is discretized on two layers of the same thickness Θ. In the sequel, subscript 1 denotes the upper layer, and subscript 2 the lower layer. The discretized potential vorticity now becomes

$$q_1 = f_0 + \beta y + \Delta\psi_1 + R_1^{-2}(\psi_2 - \psi_1) \quad (2.3a)$$

$$q_2 = f_0 + \beta y + \Delta\psi_2 + R_2^{-2}(\psi_1 - \psi_2) \quad (2.3b)$$

where R_1 and R_2 are the internal Rossby deformation radii in the two layers. We have assumed free surfaces at the top and bottom boundaries and an infinite external radius.

The model geometry is a reentrant channel of length $L = 28\,000$ km and width $D = 7000$ km, centered at 45°N, with $f_0 = 10^{-4}\ s^{-1}$ and $\beta = 1.6 \times 10^{-4}\ m^{-1}\ s^{-1}$. The lateral boundary conditions are periodic in longitude and free slip at $y = \pm D/2$. The vertical constants are derived from the U.S. Standard Atmosphere (Berry et al. 1973), with bottom temperature $\theta_B = 288$ K and top temperature $\theta_T = 328$ K [$p_s(\theta_B) = 101.5$ kPa and $p_s(\theta_T) = 24$ kPa], giving rise to $R_1 = 500$ km and $R_2 = 707$ km.

Within each layer, the streamfunction is expanded into a mean flow component and a spectral sum of Fourier harmonics, i.e.,

$$\psi_i(x, y, t) = -U_i(t)y + \sum_{m=1}^{M}\sum_{n=-N}^{N}\psi_{mn}^{(i)}(t)e^{2i\pi n(x/L)}\sin(\pi my/D) \quad (2.4)$$

with $\psi_{mn}^{(i)} = -\psi_{mn}^{*(i)}$. The use of lateral sine modes in Eq. (2.4) for both zonal and nonzonal components is nonorthodox and at first sight infringes the Phillips condition. (See appendix A for a discussion of this point.) The truncation of the spectral expansion is fixed at $M = 13$ and $N = 21$ after testing that the inclusion of further small-scale modes does not affect the large-

scale dynamics. The nonlinear Jacobian is computed without aliasing by Fourier transforms on a collocation grid with 64 × 20 points in longitude and latitude, respectively.

The forcing is chosen in order to maintain a basic flow that reproduces the main features of the average atmospheric midlatitude wintertime circulation. We first fix a uniform wind in each layer with values $U_1 = 6$ m s^{-1} in the lower layer and $U_2 = 18$ m s^{-1} in the upper layer, which both turn out to be very realistic (cf. Oort 1983). A consequence of this setting is that the external mode (3, 2) is close to stationarity. Physically, we require that the ageostrophic northward flux of momentum compensates for the Ekman dissipation of momentum in the channel (there is no orographic drag), and that the heat flux maintains a constant uniform mean shear. The second component of the forcing breaks the zonal symmetry by the introduction of a localized baroclinic jet, designed to imitate the Atlantic or Pacific jets. More precisely, the total basic flow is defined as

$$\psi_1^* = -U_1 y + A^* g(x) h(y) \tag{2.5a}$$

$$\psi_2^* = -U_2 y \tag{2.5b}$$

where $g(x)$ and $h(y)$ are described shortly. The forcing terms G_1 and G_2 in the discretized version of Eq. (2.2) are such that they maintain $\psi^* = (\psi_1^*, \psi_2^*)$ as a stationary solution of the model equations. The meridional structure of the localized component is

$$h(y) = y(y - D)\left(y - \frac{D}{2}\right), \tag{2.6}$$

so that $\partial h/\partial y$ has a maximum at $y = D/2$ and $h(0) = h(D) = 0$. The zonal structure is given by

$$g(x) = \begin{cases} g_0 \quad \text{if} \quad L \geq x \geq \dfrac{1}{4}L & (2.7a) \\ g_0 + (1 - g_0)\left(\left(\dfrac{x}{L} - \dfrac{1}{8}\right)^2 - \left(\dfrac{1}{8}\right)^2\right)^2 \Big/ \left(\dfrac{1}{8}\right)^4 & \\ \qquad \text{if} \quad \dfrac{1}{4}L \geq x \geq 0. & (2.7b) \end{cases}$$

When $g_0 = 0$, the sole inhomogeneity of the basic field lies in the first quarter of the channel. However, preliminary experiments performed with $g_0 = 0$ have shown that lateral boundaries are likely to produce spurious reflections of baroclinic disturbances and that small positive values of g_0 induce a significant focusing effect inside the channel. It appears that a convenient value is $g_0 = 0.1$ for which Fig. 1 shows the total basic streamfunction ψ_1^*. The amplitude A^* is computed in such a way that the maximum shear at the center of the jet is 37 m s^{-1}, which again turns out to be close to observed values for the Northern Hemisphere winter. In the eastern part of the channel, the shear varies from 14.5 m s^{-1} at $y = D/2$ to 7 m s^{-1} at $y = 0$ and $y = D$. The localized increase of vertical shear is expected to provide a local source of baroclinic instability which, in turn, determines the characteristics of growing disturbances as suggested by Pierrehumbert (1984). But, as discussed in section 6, the existence of an unstable mean shear over the whole channel is necessary to obtain realistic wave activity.

The dissipation incorporates four different mechanisms and reads:

$$E_1 = -\nu_1{}^i \Delta(\psi_1 - \psi_2) + \alpha \frac{\partial^8 q_1}{\partial x^8} + \alpha' \frac{\partial^8 q_1}{\partial x^8} + D_p(q_1)$$

$$E_2 = -\nu_2{}^i \Delta(\psi_2 - \psi_1) - \nu^e \Delta\psi_2 + \alpha \frac{\partial^8 q_2}{\partial x^8} + \alpha' \frac{\partial^8 q_2}{\partial y^8} + D_p(q_2),$$

where

1) The Ekman damping $-\nu^e \Delta\psi_2$ acts in the bottom layer with $1/\nu^e = 4$ days.

2) The internal friction acts differently in the two layers because the deformation radii are different. The ratio $\nu_1{}^i/\nu_2{}^i$ must be equal to $R_2{}^2/R_1{}^2$ to ensure that the process is dissipative in all cases and that the vertical integral of the potential vorticity is conserved. In the upper layer, $1/\nu_1{}^i = 7$ days, and in the lower layer, $1/\nu_2{}^i = 35$ days.

3) The superviscosity damping characterized by the factors α and α' acts selectively on the tail of the spectrum; α and α' are chosen such that both zonal and meridional cut-off modes ($n = N = 21$, $m = M = 13$) are damped with a damping time of 2.8 h.

4) The additional damping terms $D_p(q_1)$ and $D_p(q_2)$ act selectively in both layers on the first zonal planetary modes $(0, m)$, $(1, m)$, $(2, m)$ and $(3, m)$ with $m = 1, \cdots, M$. The associated damping times are 12 days for mode 0, 17 days for mode 1, 23 days for mode 2 and 29 days for mode 3. Although small, this damping is necessary to avoid excessive accumulation of energy on these modes. It accounts for the Newtonian cooling and the lack of vertical propagation towards the stratosphere, and lack of horizontal propagation towards the tropics which is inherent to our model; these mechanisms preferentially affect the largest zonal atmospheric scales (Held 1983).

Time stepping is performed using a predictor–corrector scheme. The numerical model code is able to simulate 100 days in about 50 s CPU of Cray1 with a time step of 1 h.

3. Linear instability

As a first step in the analysis of our model, and because we want to assess the role of nonlinear vs linear dynamics, we investigate the behavior of small amplitude perturbations of the basic state using linear ap-

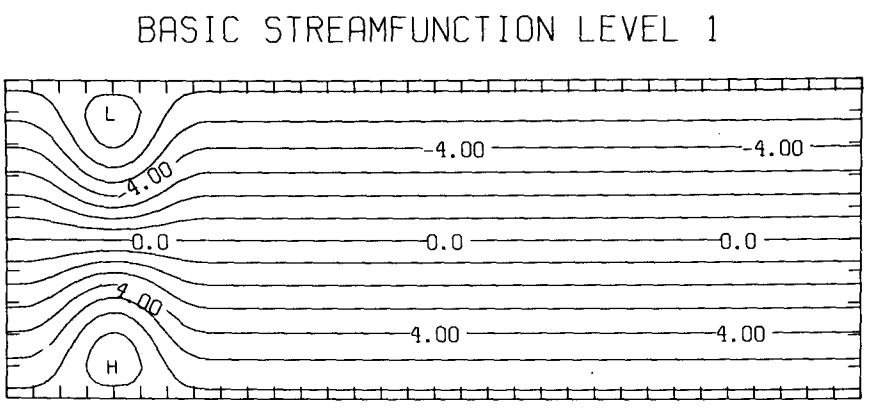

FIG. 1. Contours of the basic streamfunction ψ_1^* in the upper layer. Units 10^7 m^2 s^{-1}.

proximation. For $A^* = 0$, the basic flow is zonally homogeneous and the eigenvalue problem reduces to the classical Philips problem. The most unstable modes are the symmetric components (7, 1) and (8, 1) with periods and e-folding times of about 5 days.

As previously discussed, the mean zonal wind is chosen so that the external mode (3, 2) is close to stationarity. This mode has a period of more than 1000 days and a negative e-folding time of -5 days. Long periods are exhibited by other external modes: for instance, the modes (4, 1) (20 days) and (5, 1) (34 days). It must be noted that the quasi-stationary external mode (3, 2) is more stable than its internal counterpart having an e-folding time of -13 days. This property is quite general. That is, for a given two-dimensional wavenumber (n, m), the external mode (almost barotropic) is generally more stable than the internal mode (tilted with height). However, the long periods of barotropic large-scale modes make them more likely to respond to strong enough stationary forcing.

For the nonparallel basic flow with $A^* \neq 0$, the linear eigenmodes are numerically computed. The fastest growing modes bear strong similarities with the most unstable modes of the homogeneous problem. However, e-folding times are reduced, as well as periods, as a consequence of the vertical shear and zonal wind increases in the jet. An instantaneous pattern of the fastest growing mode is shown in Fig. 2. It exhibits a dominating structure (7, 1) in wavenumber and a westward tilt with height, so that the two layers are almost out of phase. Phase variations at central latitude are leading phase variations at boundaries, owing to the slight focusing effect introduced in ψ^*.

Through an appropriate translation of time origin, the time evolution of an eigenmode reads

$$\psi_i(x, y, t) = \left(\phi_i^c(x, y) \cos\left(\frac{2\pi t}{T}\right) + \phi_i^s(x, y) \sin\left(\frac{2\pi t}{T}\right)\right) e^{t/\tau}, \quad (3.1)$$

which can be transformed into an equivalent form

$$\psi_i(x, y, t) = \sqrt{v(x, y)}\ \mathrm{Re}(e^{i[(2\pi t/T) - \phi(x,y)]}) e^{t/\tau}. \quad (3.2)$$

Assuming that the mode saturates at a given amplitude, i.e., removing the exponential factor from (3.2), $v(x, y)$ can be interpreted as a local variance of the eigenmode and $\nabla\phi(x, y)$ as a local wavevector. Figure 3 shows both quantities for the most unstable mode in the upper layer. The maximum of the variance occurs at the exit of the jet and this region is also associated with a splitting of the perturbations. Within the jet, the local wavenumber is about 5 whereas it turns out to be 7 elsewhere. This effect is easily explained by the local increase of phase velocity within the jet while the period of the oscillation remains constant. These results are in good agreement with the findings of Frederiksen (1982), although our modes are less local than his. Particularly, we find dipolar modes with periods between 4 and 12 days and e-folding times from 6 to 15 days. They are less unstable than those found by Frederiksen and exhibit a global structure. They cannot be associated with "onset of blocking" as he suggested.

The addition of zonal inhomogeneity in baroclinity introduces another difference with respect to the homogeneous case: the existence of a local mode which is stationary and unstable, with an e-folding time of 11 days. This eigenmode is not affected by variations of the mean zonal wind and mean vertical shear, and even exists when $U_1 = U_2$, although its shape is slightly modified. This is evidence for associating it not with a standard baroclinic instability but rather with a direct response to local forcing. Its spatial pattern, shown in Fig. 4, turns out to be remarkably localized. The baroclinity is entirely contained in the meridional direction. When the sign of the perturbation is positive, this mode acts to amplify the jet and to extend it downstream in the upper level, and to create a wide westerly jet in the lower layer with a strong return current at lateral boundaries. It then contributes to increase the baroclinity in the center of the channel and slightly downstream from the basic jet maximum.

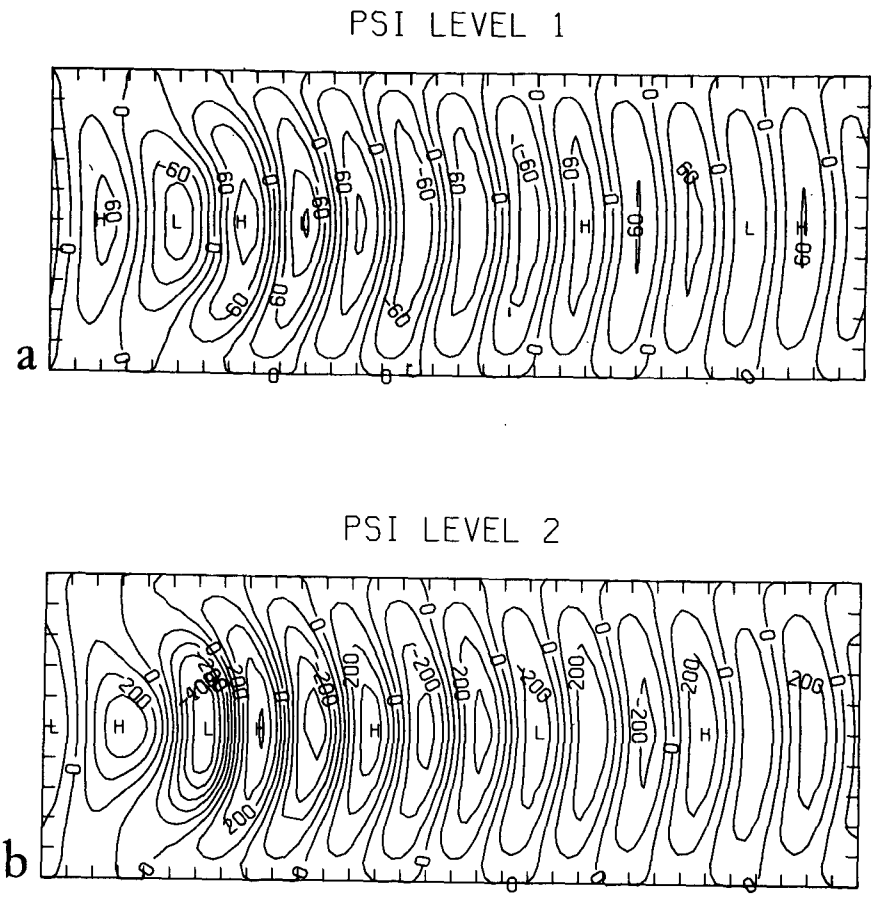

FIG. 2. Instantaneous streamfunction for the fastest growing mode of the perturbation around the basic state Ψ^*. (a) Upper layer, and (b) lower layer. Arbitrary units.

It is questionable whether the nonlinear feedback of most unstable propagating perturbations can excite the unstable stationary mode. For a given baroclinic eigenmode, this feedback can be worked out by averaging over the phase, as for the variance (see also Frederiksen 1982). Figure 5 shows the upper-layer streamfunction associated with the nonlinear feedback of the most unstable eigenmode. Comparing with Fig. 4 demonstrates that the feedback is able to excite the unstable stationary mode with a positive sign. The growth of this mode

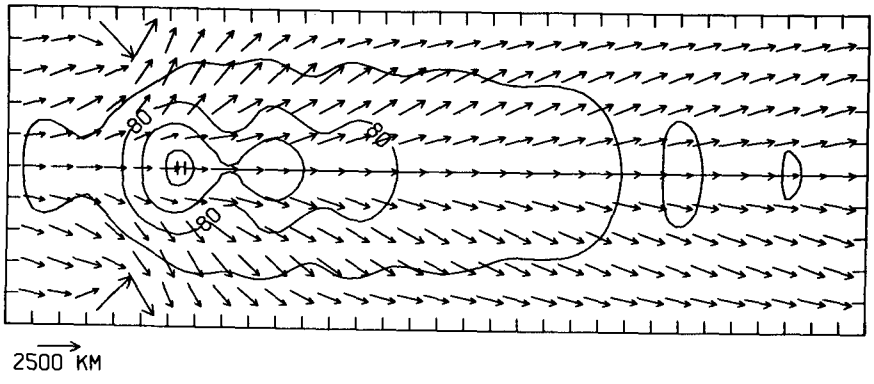

FIG. 3. Contours show the variance of the first eigenmode streamfunction in the upper layer. Arrows indicate the local direction of phase velocity and their modulus can be interpreted as the local wavenumber. The reference arrow plotted in the lower left corner is associated with a wavelength of 2500 km. The phase gradients were computed using a 64 × 20 grid but are shown on a 32 × 9 grid.

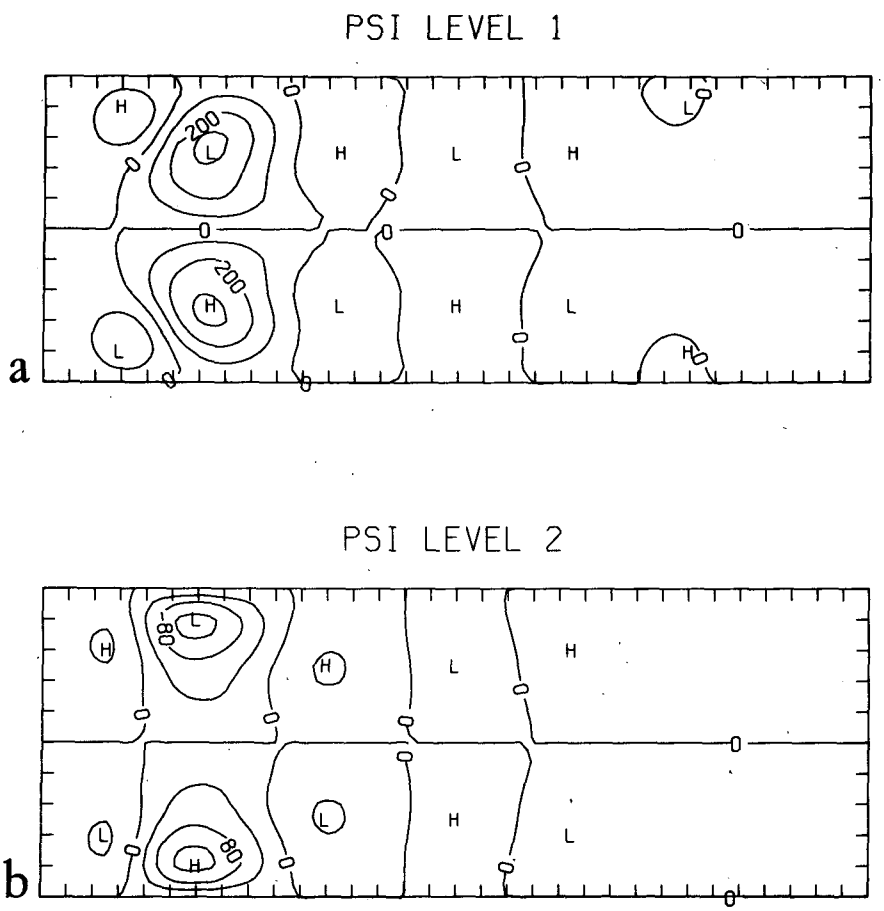

FIG. 4. As in Fig. 2 except for the unstable stationary mode.

can then only be stopped by nonlinear interactions when its amplitude reaches a large enough value. We thus expect a large contribution to the averaged flow of the nonlinear model, as section 4 shows. The feedback shown in Fig. 5 also tends to directly force a splitting at the exit of the jet and the other most unstable eigenmodes give similar contributions to the unstable stationary mode.

4. Flow statistics

The results presented in this section and in section 5 are based on three long-term integrations (A, B and C) of the model of 15 000 days each. Data are sampled once a day and stored as Fourier coefficients and also as values on a 32 × 9 grid in longitude and latitude. In the following we will often refer to positions on this

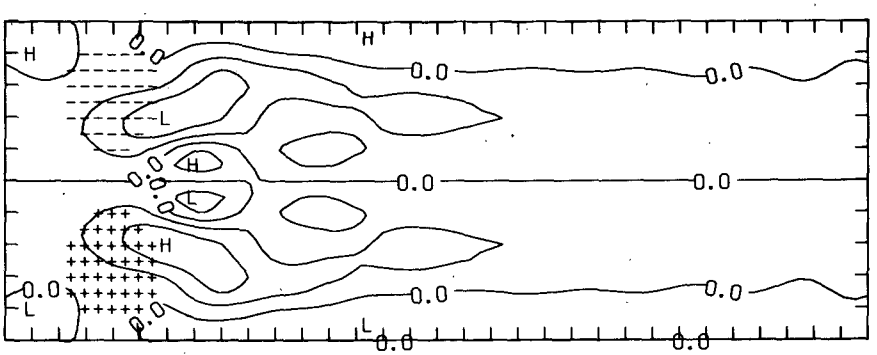

FIG. 5. Upper-layer streamfunction associated with the nonlinear feedback of the most unstable mode. The basic jet anomaly pattern is identified by the two patches of minus and plus signs.

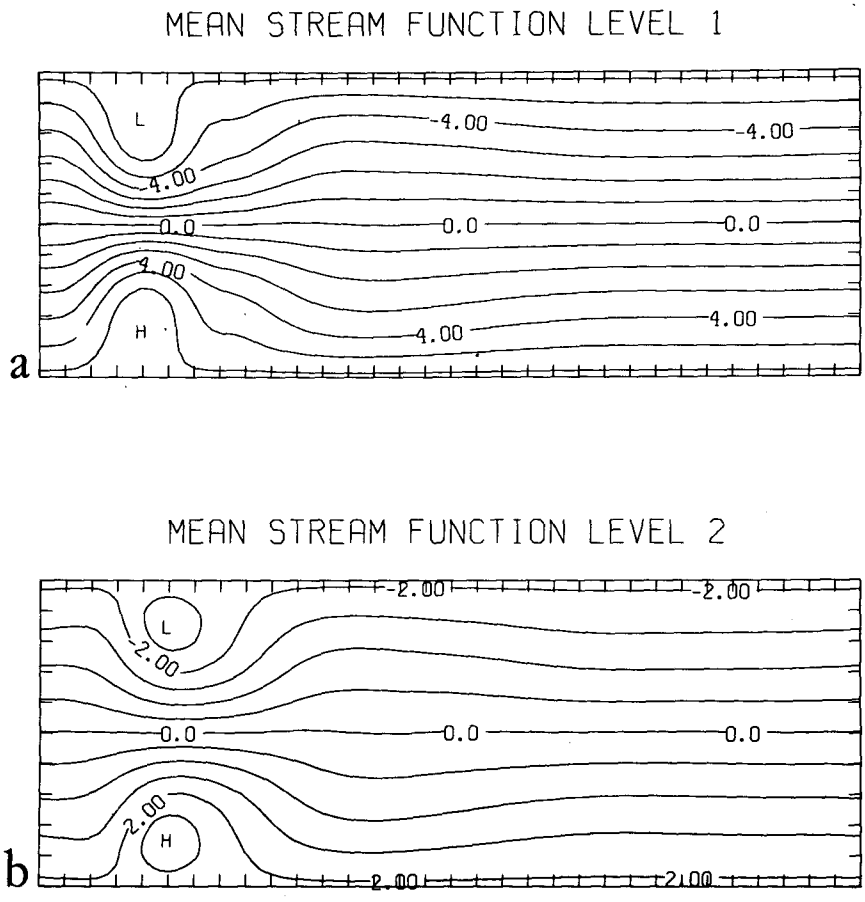

FIG. 6. Averaged streamfunction over the 15 000 days of experiment A. (a) Upper layer, and (b) lower layer. Units 10^7 m^2 s^{-1}.

grid; they are indicated with tick marks in all figures showing spatial fields (e.g., Fig. 1).

a. Global averages

Figure 6 shows the average flow over the 15 000 days of experiment A. The dominating pattern is a centered jet in both layers which extends somewhat downstream from the basic forced field in the upper layer (Fig. 1). The maximum values of the zonal wind, 45 m s^{-1} in the upper, and 15 m s^{-1} in the lower layer, are in good agreement with wintertime atmospheric data. We correctly simulate the vertical westward tilt of the maximum wind shown in Oort (1983). However, the well-known horizontal northward tilt is missing, owing to the imposed symmetry of the channel. The pattern of the difference between the mean flow and ψ^* resembles the unstable barotropic mode shown in Fig. 4 as conjectured in section 3. In particular, the lower-level mean jet is well in phase with the pattern of Fig. 4b. Moreover, the linear stability study of the mean flow does not reveal any comparable unstable of marginally stable barotropic eigenmode, confirming the existence of a nonlinear saturation of the stationary instability of the basic flow.

The total variance of the streamfunction, Fig. 7, concentrates at the exit of the jet and exhibits a diffluent structure with two secondary symmetrical maxima in the second zonal quarter of the upper layer, while in the lower layer, the main centered maximum disappears. The dominating source of variability lies obviously in the localized region of high baroclinity and the largest part of the activity is observed within the first half of the channel, thus limiting the possible resonance effects that the periodic boundary conditions may induce.

Figure 8 shows the temperature variance together with the eddy heat fluxes $\overline{v'T'}$ where the primes denote the departure from the time average (overbar). Eddies act mainly to destroy the imposed temperature gradient. As in the atmosphere, the largest fluxes are directed northwards in the upstream part of the active domain and have negligible effects downstream. Notice also that significant fluxes occur along channel boundaries, but they produce a negligible heating.

Figure 9 shows the vertically averaged potential vor-

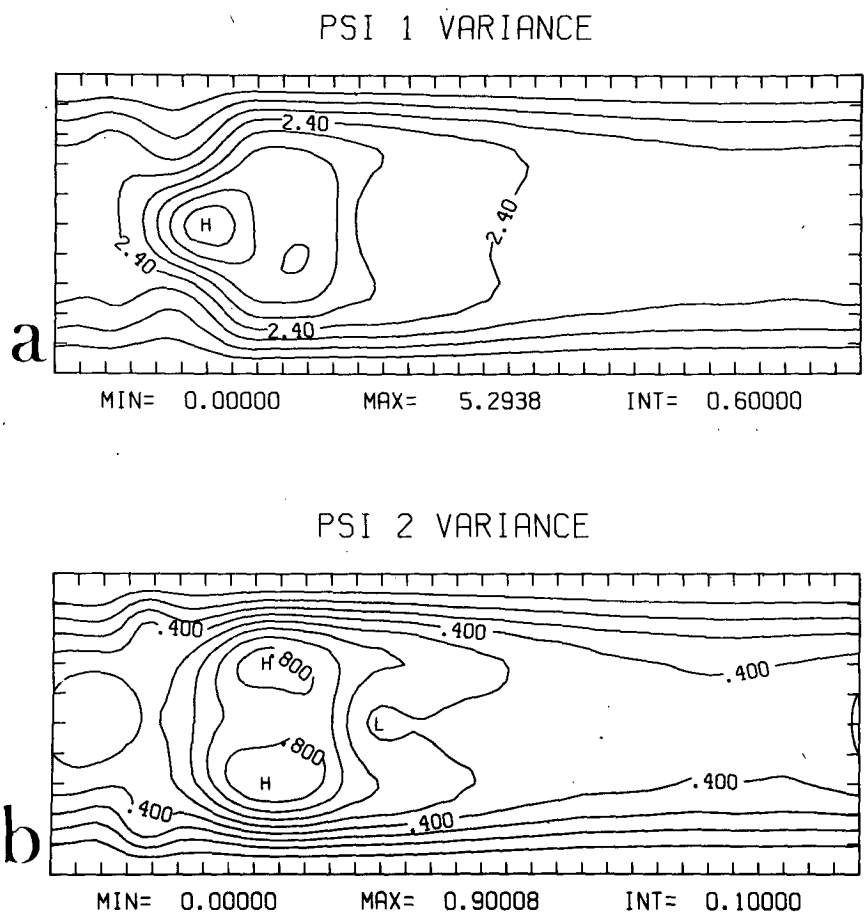

FIG. 7. Total variance of the streamfunction averaged over experiment A. (a) Upper layer, and (b) lower layer. Units 10^{14} m^4 s^{-2}. Contour interval (a): 0.6 10^{14} m^4 s^{-2} (b): 10^{13} m^4 s^{-2}.

ticity flux $\frac{1}{2}(\overline{\mathbf{v}_1'q_1'} + \overline{\mathbf{v}_2'q_2'})$. The flux roughly follows the contours of the potential vorticity variance (not shown), as observed by Lau and Wallace (1979) in the atmosphere. Figure 9 also shows the resulting forcing on the streamfunction field. More precisely, we apply to the eddy vorticity forcing $(-\nabla\cdot\overline{\mathbf{v}_1'q_1'}, -\nabla\cdot\overline{\mathbf{v}_2'q_2'})$ the linear operator which transforms (q_1, q_2) into (ψ_1, ψ_2), and we average the result over the two layers. The visible effect in Fig. 9 is to damp the jet where it is a maximum and to extend it somewhat upstream and more strongly downstream. As for the heat flux, no significant forcing is produced on the boundaries.

b. *Propagative and stationary variance*

Following Hayashi (1971), we consider the longitude–time spectra of the upper-level streamfunction at a given latitude. We take 75 samples of 200 consecutive days; on each, we perform the time Fourier transform of the longitude Fourier coefficients. If $\psi'(x, t)$ is the streamfunction anomaly [with respect to the 15 000-day average $\bar{\psi}(x)$] and the associated spectral coefficients, $c(k, a)$ are given by

$$c(k, \omega) = \frac{1}{200}\sum_{t=1}^{200} e^{-i2\pi\omega t}\left[\frac{1}{32}\sum_{m=1}^{32}\psi'\left(\frac{2\pi m}{32}, t\right)e^{i2\pi mk/32}\right], \tag{4.1}$$

and conversely

$$\psi'(x, t) = \sum_{k=0}^{16} a_k \sum_{n=-99}^{100}\left[c_r\left(k, \frac{n}{200}\right)\cos\left(\frac{2\pi nt}{200} - kx\right) - c_i\left(k, \frac{n}{200}\right)\sin\left(\frac{2\pi nt}{200} - kx\right)\right], \tag{4.2}$$

where $a_0 = a_{16} = 1$ and $a_k = 2$ for $0 < k < 16$. We utilize the data archived on the 32×9 grid (see above). Westward (eastward) propagation corresponds to positive (negative) values of the frequency ω. Thus for a given sample, an estimate of the variance of the mode (k, ω) is $a_k\,|\,c(k, \omega)\,|^2$. The two-sided variance spectrum $E(k, \pm\omega)$ is computed by averaging over the 75 estimates. We observe a small variance between the estimates showing that the features we are discussing

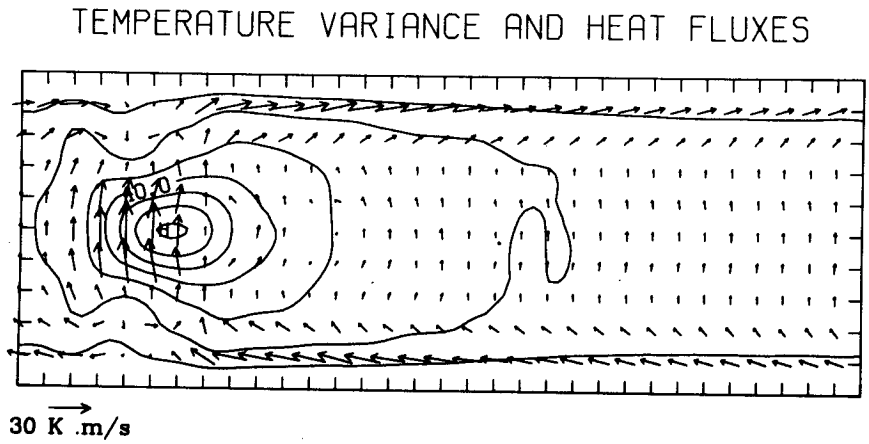

FIG. 8. Temperature variance (in K^2) and eddy heat fluxes $\overline{v'T'}$ averaged over experiment A. The scale for the fluxes is given in the lower left corner. Contour interval 10 K^2.

are highly significant. The spectra are calculated at latitude 7, at ¾ of the channel width, and therefore capture the oscillations of the zonal velocity along the channel axis. Following Pratt (1976) and Fraedrich and Böttger (1978) the two-sided spectrum $E(k, \pm\omega)$ may be separated into a propagating spectrum defined as

$$PR(k, \omega) = |E(k, \omega) - E(k, -\omega)|, \quad (4.3)$$

with the convention that eastward propagation corresponds to $E(k, \omega) > E(k, -\omega)$, and a stationary spectrum

$$SR(k, \omega) = 2 \text{ Min}(E(k, \omega), e(k, -\omega)). \quad (4.4)$$

Figure 10 shows these one-sided variance density spectra as a function of longitudinal wavenumber and period at latitude 7. Comparisons can be performed with the results of Fraedrich and Böttger (1978) who calculated the same quantities for five winter seasons (1972–77) of the daily 50 kPa geopotential fields at 50°N. The propagating variance, Fig. 10a, shows a weak westward propagation at low wavenumbers and a maximum eastward propagation at wavenumber 6, with a period of 5–9 days, which is in agreement with observations. (Fraedrich and Böttger found two maxima at period 5 and 8.) The stationary variance, Fig. 10b, is less dispersive, and the maximum is found for wavenumber 4 and period 20–30 days though Fraedrich and Böttger found the maximum at wavenumber 3. The same analysis for the antisymmetrical part of the fields, Fig. 10c, shows that the stationary variance is essentially concentrated within zonal modes 1, 2 and 3 with a peak at wavenumber 2, and no energy at wavenumber 4. Thus, the maximum found at wavenumber 4 for the total variance is due to a symmetric oscillation which is presumably linked with a stationary, marginally stable, global eigenmode (Vautard 1987). The main result arising from Fig. 10 is the clear separation between low-frequency, stationary variance

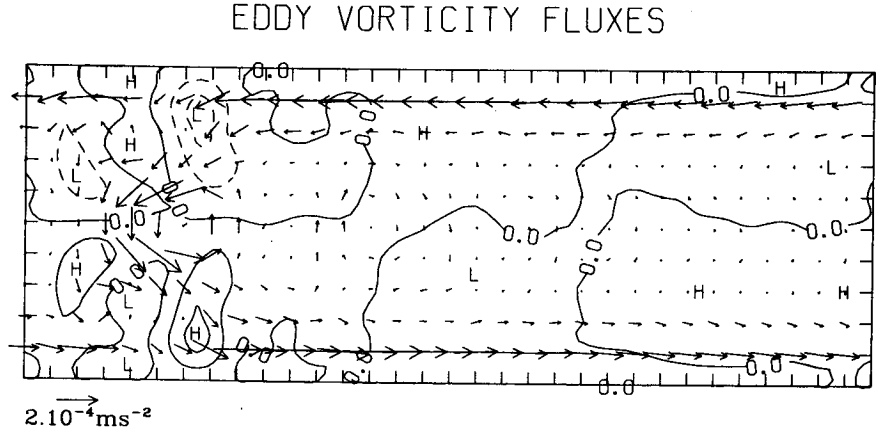

FIG. 9. Vertically averaged potential vorticity fluxes $\frac{1}{2}(\overline{v_1'q_1'} + \overline{v_2'q_2'})$ and the resulting forcing on the streamfunction field. (See section 4 for explanations.) The scale for the fluxes is given in the lower left corner. Contour interval 10 $m^2 s^{-2}$.

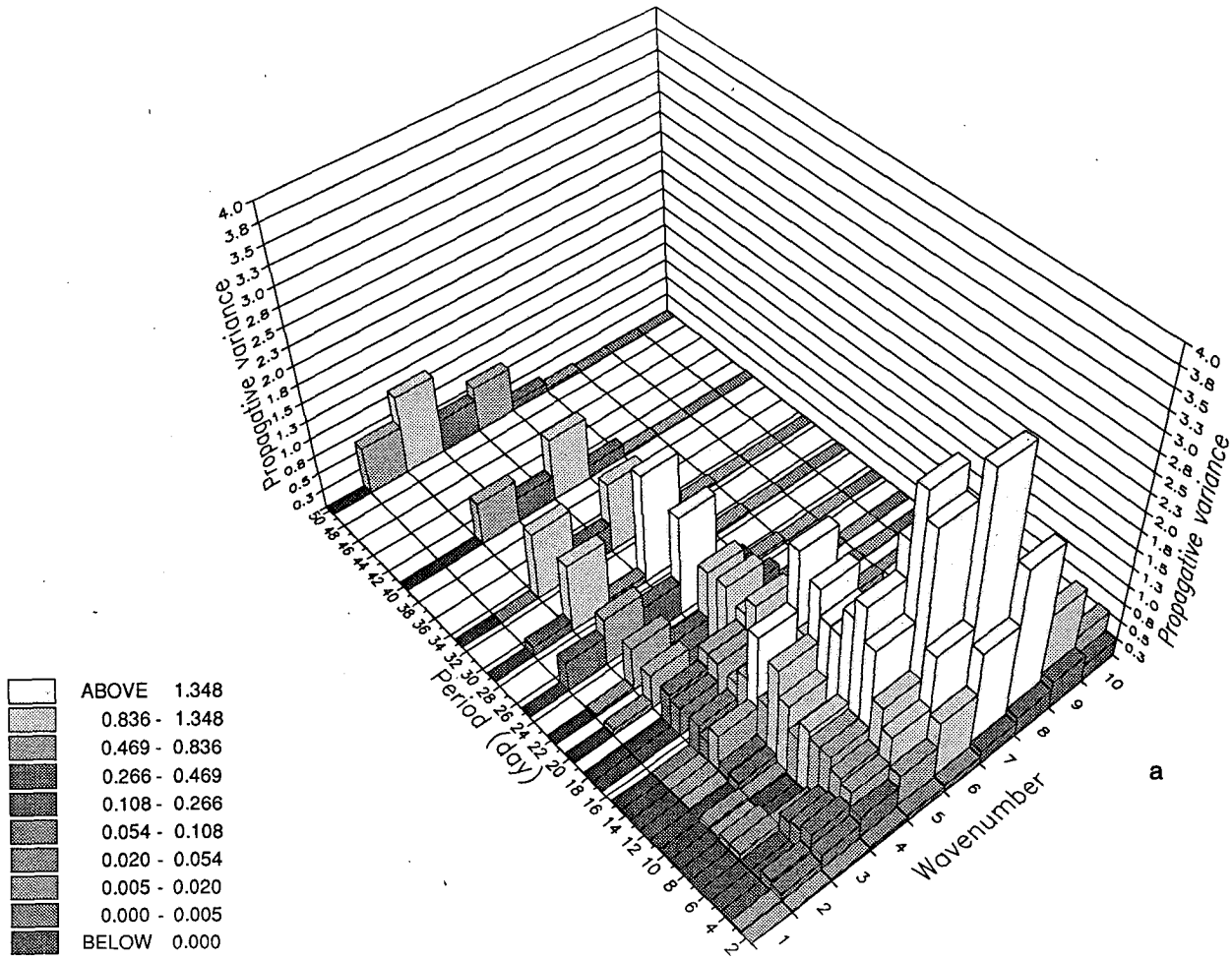

FIG. 10. (a) Propagating and (b) stationary variance spectrum of the upper-layer streamfunction at latitude 7 as a function of the longitudinal wavenumber and of the period. The spectrum is originally computed as a function of the frequency and is summed within temporal boxes of width 1 day along the period axis. Empty boxes (because of the frequency sampling) are blanked. (c) The stationary variance computed over the antisymmetrical part of the field.

associated with large scales and high-frequency, propagating variance associated with synoptic scales. The scale separation used later in this study relies on that feature. However, the drawback of space–time spectral analysis is that the method detects preferentially global regular phenomena of relatively weak amplitude rather than the local high amplitude variability we are interested in.

The *complex principal component analysis* (CPCA) we are going to describe complement the latter analysis since it provides more information on the spatial structure although it does not say much about scale separation. We follow the approach of Barnett (1983) which generalizes the *principal component analysis* (PCA) [or *empirical orthogonal function analysis* introduced by Lorenz (1956)]. Let $\hat{\psi}'(\mathbf{x}, t)$ be the Hilbert transform (cf. Thomas 1969) of the geopotential field $\psi'(\mathbf{x}, t)$ with respect to time. If we perform a (complex) PCA on the new field $\psi'_c = \psi' + i\hat{\psi}'$, we get the expansion

$$\psi'_c(\mathbf{x}, t) = b_1(t)e^{i\varphi_1(t)}B_1(\mathbf{x})e^{i\phi_1(\mathbf{x})} + \cdots + b_n(t)e^{i\varphi_n(t)}B_n(\mathbf{x})e^{i\phi_n(\mathbf{x})} + R_n(\mathbf{x}, t) \quad (4.5)$$

where $B_j(\mathbf{x})e^{i\phi_j(\mathbf{x})}$ is the jth eigenvector or *complex empirical orthogonal function* (CEOF) of the covariance matrix of ψ'_c and $b_j(t)e^{i\varphi_1(t)}$ is the projection of ψ'_c onto this vector. In this way, the truncation error R_n possesses a minimal mean square modulus. Taking the real part of (4.5) gives

$$\psi'(\mathbf{x}, t) = b_1(t)B_1(\mathbf{x})\cos[\varphi_1(t) + \phi_1(\mathbf{x})] + \cdots + b_n(t)B_n(\mathbf{x})\cos[\varphi_n(t) + \phi_n(\mathbf{x})] + R_{nr}(\mathbf{x}, t), \quad (4.6)$$

which is a generalization of the PCA expansion:

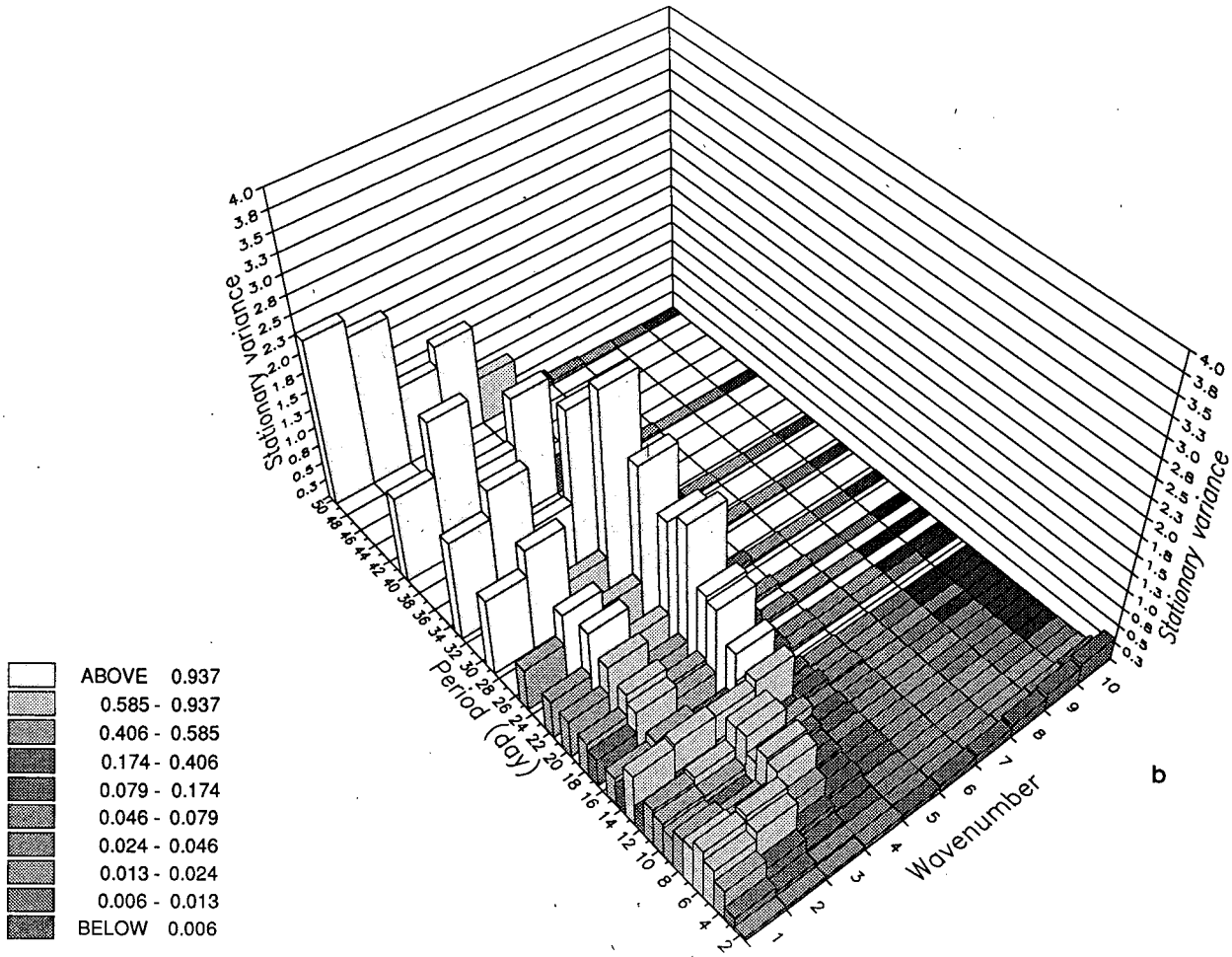

FIG. 10. (*Continued*)

$$\psi'(\mathbf{x}, t) = a_1(t)A_1(\mathbf{x}) + \cdots + a_n(t)A_n(\mathbf{x}) + S_n(\mathbf{x}, t). \quad (4.7)$$

The covariance matrix of ψ'_c, $W(\mathbf{x}, \mathbf{x}')$ (which is four times the cospectral matrix of ψ'), has been calculated in the same way as the longitude–time spectra; 75 estimates of $W(\mathbf{x}, \mathbf{x}')$ are calculated for each $\mathbf{x}$ and $\mathbf{x}'$ by time Fourier transforms over 200-day series, and their average is considered as the expectation of the cospectrum. The eigenvectors $B_j(\mathbf{x})e^{i\phi_j(\mathbf{x})}$ and the corresponding scores $b_j(t)e^{i\varphi_j(t)}$ are chosen so that the mean square of $b_j(t)\cos[\varphi_j(t) + \phi_j(\mathbf{x})]$ is 1. The mean square of $B_j(\mathbf{x})$ divided by the mean square of $\psi'(\mathbf{x}, t)$ thus gives the part of the variance explained by the jth CEOF. The daily phase trend $\varphi_j(t-1) - \varphi_j(t)$ when averaged over a 200-day sample yields an estimate of the period T_j of the oscillation. The average $\bar{T}_j$ and the standard deviation σ_j of T_j over the 75 estimates indicate how regular the time evolution of the pattern is. When the period is sufficiently stable (i.e., $\sigma_j \ll \bar{T}_j$) we can compute a local phase velocity $\mathbf{v}_j(\mathbf{x}) = -(2\pi\nabla\phi_j(\mathbf{x}))/(\bar{T}_j\|\nabla\phi_j(\mathbf{x})\|^2)$ associated with the local wave vector $\mathbf{k}_j(\mathbf{x}) = -\nabla\phi_j(\mathbf{x})$. Using 200-day samples is sufficient to study phenomena with time scales smaller than 50 days. The results discussed below are not modified up to the third CEOF when calculations are based on 100 or 300 days series. Similar results are also obtained when only the first or the last 7000 days of the experiment are considered.

The first CEOF, Fig. 11a, exhibits a period of 10 days which is very stable (standard deviation is 1 day). It explains 11.4% of the variance and is associated with symmetrical disturbances propagating eastwards between longitude 5 and longitude 10 along the channel axis. Fluctuations in the meridional velocity behave with a local wavenumber 4–5 and a local phase velocity of 8 m s^{-1} measured in the eastern part of the channel. A comparison with the most unstable mode arising from linear analysis (Fig. 3) demonstrates a wavenumber and frequency decrease due to the nonlinearity of the dynamics. An analogous shift is observed by Simmons and Hoskins (1978), and by Frederiksen (1982)

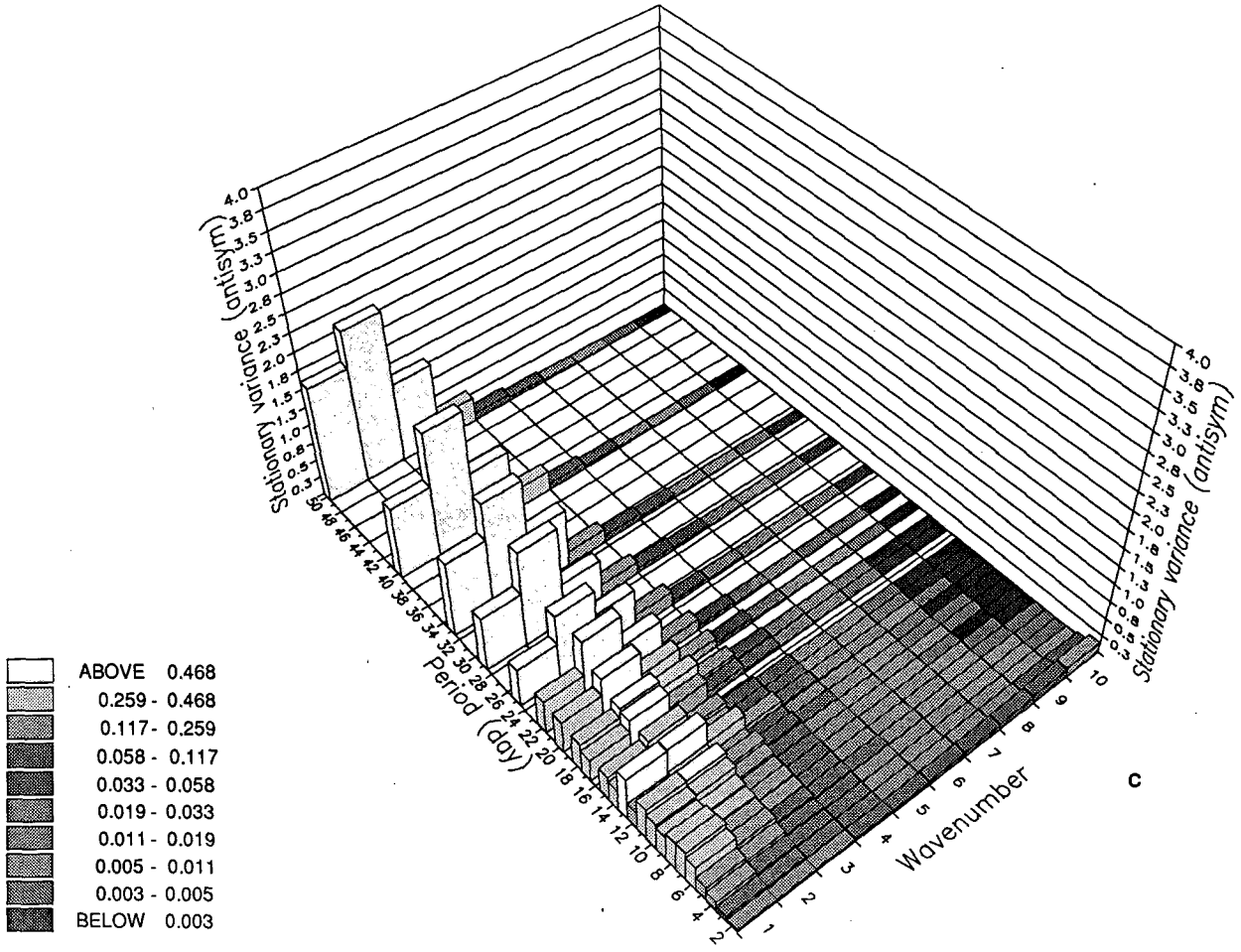

FIG. 10. (*Continued*)

who compares the dynamics of linear perturbations and the transient statistics measured by Blackmon et al. (1977).

The second CEOF, Fig. 11b, is antisymmetrical and exhibits a dipolar amplitude maximum at longitude 10 and explains 7.8% of the total variance. The period of 30 days is much longer than previously, but is also fluctuating largely (standard deviation is 10 days). One can also observe in Fig. 11b, at latitudes 3 and 7, that the phase velocity decreases when the longitude increases, i.e., that the dipole slowly moves eastwards with an average phase velocity of about 4 m s^{-1}. However, the significance of this propagation is questionable since the period of the oscillation is not well defined.

c. *Large- and small-scale dynamics*

The total variance maps shown in Fig. 7 do not allow the distinction between the contributions from different temporal and spatial scales involved in the dynamics. It is now classic (Blackmon 1976; Blackmon et al. 1977) to filter atmospheric data in order to separate synoptic-scale activity from low-frequency variability. Since these two domains separate in both space and time, (cf. Fig. 10) wavenumber and frequency filterings should yield two similar results. Our choice is to perform a cut in wavenumber domain: the large-scale part of a given field is defined as its truncated Fourier expansion with zonal wavenumbers $[0, N_L]$ and meridional wavenumbers $[1, M_L]$. The small-scale component is defined as the complementary part, so that the vorticity field (for instance) can be decomposed as

$$q_i = q_i^L + q_i^s \quad \text{with} \quad i = 1, 2. \tag{4.8}$$

The stationary and propagative frequency–wavenumber spectra of Fig. 10 suggest a zonal separation scale at $N_L = 3$ or 4, while the meridional separation scale is undetermined. In order to reduce as much as possible the dimension of the space used to describe the low-frequency variability, we choose $M_L = 2$, so that only two kinds of large-scale waves are retained: the symmetric waves with meridional wavenumber 1

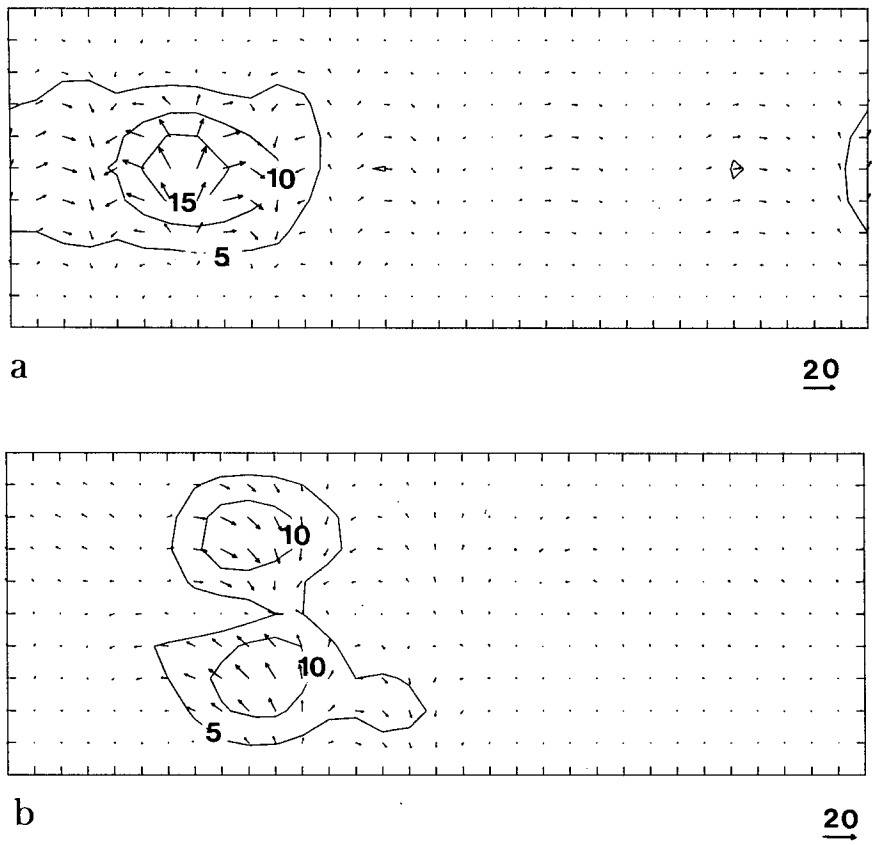

FIG. 11. (a) First and (b) second CEOF of the upper-level streamfunction. The arrow length and the isolines (units 10^6 m^2 s^{-1}) are related to the modulus of the CPC. The angle between the arrow and the channel axis gives the phase.

and the antisymmetric waves with meridional wavenumber 2.

Vautard (1987), hereafter V87, compares the two choices, $N_L = 3$ and $N_L = 4$, and shows that the first is suitable for the study of zonally inhomogeneous, low-frequency variability. In the following, the large-scale set of variables is further reduced by only keeping the antisymmetric meridional wavenumber 2, so that the dimension of the vector-space spanned by the large scales is 14 [1 mode (0, 2), 2 modes (1, 2), 2 modes (2, 2) and (3, 2) in each layer]. The definition of small scales is, however, left unchanged.

The large-scale variance with $N_L = 3$ (Fig. 12a) mainly concentrates within the second quarter of the channel and has maxima in two symmetric regions. This pattern is clearly linked with the oscillation between zonal and diffluent flows already described by CPCA. Figure 12b shows the associated small-scale variance in the upper layer. It shows a clear axial storm-track pattern which extends well downstream from the exit of the jet with a maximum near its western end. Comparing Figs. 12a and b shows that, as in the atmosphere, the low-frequency variability is a maximum at the end of the storm-track. This strongly suggests that the quasi-stationary long waves may draw their energy from the transients baroclinic propagative waves through nonlinear processes.

In order to dispel the impression that the time evolution of our model is very smooth, we show two sequences of three successive daily maps of the upper-layer streamfunction in Fig. 13. The situations are chosen following a criterion developed in section 5, and represent two typical cases of persistent large-scale circulation. In the first sequence (a, b, c), baroclinic waves propagate downstream from the jet along the central latitude band. In the second case (d, e, f), eddies split at the exit of the jet, the cyclonic part going southwards and the anticyclonic part going northwards. The diffluence is caused by a large-scale blocking dipole which drives the perturbations off their usual path. It is noteworthy that the eddies weaken during their propagation around the block, indicating that a part of their vorticity has been deposited within the block or dissipated.

Henceforth, we will concentrate on the study of the large-scale flow as defined above and, unless specified,

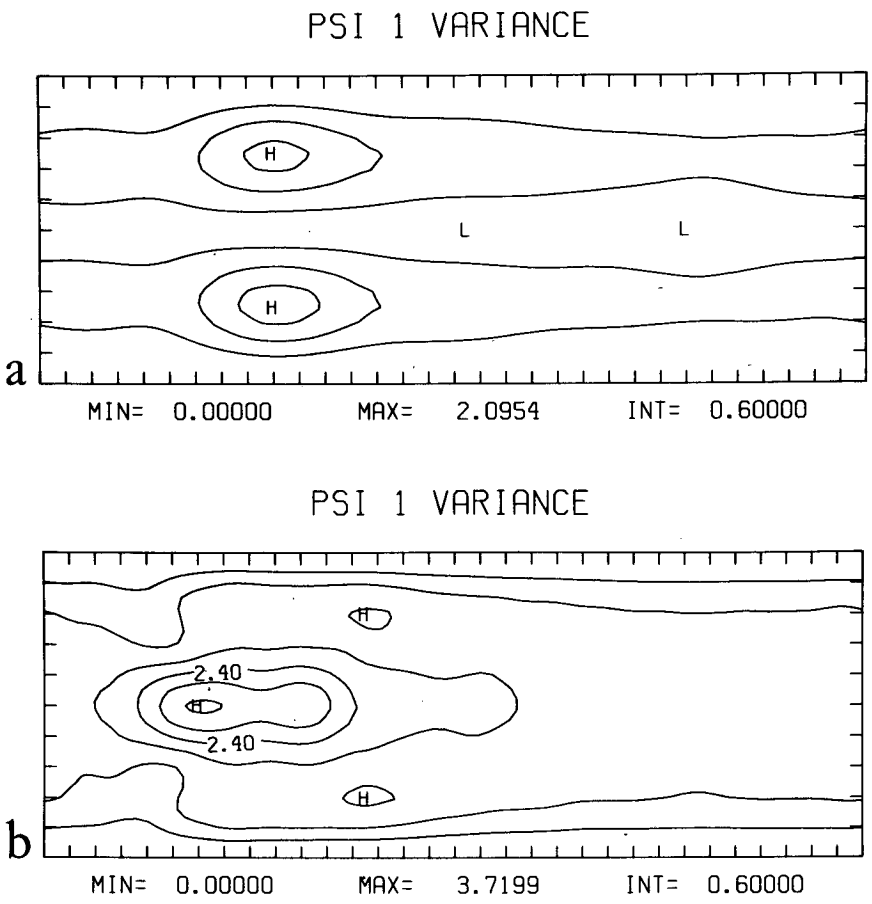

FIG. 12. (a) Large-scale variance of the upper-level streamfunction averaged over experiment A with $N_L = 3$. (b) Small-scale variance of the upper-level streamfunction. Units 10^{14} m^4 s^{-2}.

the analysis uses the full 45 000-day dataset. But 14 variables are a lot to deal with, at least for display purposes. Computing the EOFs for the time series of the upper-layer streamfunction shows that the first one explains 32% of the variance and the second one 19%, so that more than 50% of the large-scale variance is represented by the time variation of their associated *principal components* (PC). The first EOF (Fig. 14a) closely resembles the first EOF of the total field, not shown, though the second EOF (Fig. 14b) exhibits a pattern characterized by a dominant dipole downstream from the jet. These two components are used in the sequel for persistence analysis and for the display of equilibration results in Part II.

d. *Large-scale dynamics and noise*

In order to test the significance of persistence indicators developed later in section 5, we need to build up a reference stochastic model that exhibits the same variance as our model but does not incorporate explicitly its complex nonlinear dynamics. Dole and Gordon (1983) and Horel (1985) used a simple one-dimensional auto-regressive model to study the anomalies of the 50 kPa geopotential height and found significant differences between their data and the model. However, a one-dimensional process is not appropriate for a multivariate problem, because it does not take into account the cross correlations between variables and, in particular, misses propagation effects. We consider a multidimensional, first-order, auto-regressive model, based on the covariance matrix and the cross-correlation matrix at a 1-day lag. It consists of a linear auto-regression of the large-scale variables at a 1-day lag. More precisely, we take the 14 variables defining the large-scale field at a given day as predictors of the 14 variables at the next day. If X_n denotes the vector containing the variables at day n, and $\bar{X}$ the time-averaged vector, we obtain:

$$(X_{n+1} - \bar{X}) = A(X_n - \bar{X}) + R_n \qquad (4.9)$$

where A is the regression matrix and R_n the residual noise. Here, A is chosen in such a way that $A(X_n - \bar{X})$ is the least-square estimate of $\bar{X}_{n+1} - X$, and thus the variance $\overline{\|R_n\|^2}$ is a minimum.

We can now build a stochastic model (red noise) for the vector Y such that the centered vector $Y - \bar{Y}$ is a normal deviation with zero mean and the same covariance matrix as $X - \bar{X}$. Namely, we write

$$Y_{n+1} = \bar{X} + A(Y_n - \bar{X}) + W_n, \qquad (4.10)$$

where the W_n are randomly generated normal deviations with

$$\bar{W}_n = 0 \qquad (4.11)$$

$$\overline{W_n W_n^T} = \overline{R_n R_n^T}. \qquad (4.12)$$

The evolution equation (4.10) is a Markov process. Data generated through its iteration during 45 000 days show covariances and cross correlations at 1-day lag differing only by statistical estimates errors from the same quantities computed with model data. This agreement is conserved when considering only a 15 000-day series of data.

As a first application, we studied whether the distribution of positive and negative anomalies in the model dynamics differ from the red noise. We plot at latitude 7 and as a function of longitude the number of days for which the streamfunction anomaly exceeds a given threshold (similarly to Dole and Gordon 1983). Figure 15 shows the number of anomaly events as a function of longitude for model and red noise data with a threshold of 5×10^6 m^2 s^{-1} (50 m in terms of geopotential height) corresponding to weak anomalies, and 15×10^6 m^2 s^{-1} (150 m in terms of geopotential height) corresponding to large anomalies. First, the maximum of these curves corresponds well to the maximum of variance shown in Fig. 12b for both model and red noise processes. However, the model exhibits a clear asymmetry between positive and negative cases. For small anomaly values, at longitude 10, there is a clear preference for negative anomalies while the situation is reversed for strong anomalies. This feature is highly significant since, with the same amount of data, the red noise exhibits only negligible discrepancy between statistics of positive and negative anomalies. It is noteworthy that the maximum for weak positive anomalies occurs somewhat downstream from the negative maximum. All curves intersect at longitude 12 where skewness almost vanishes.

The observed asymmetry of anomalies is in agreement with the results of Dole and Gordon (1983). Zonal circulations are often associated with weak anomalies of the flow while blocking situations need a high positive anomaly (about +120 m near longitude 12) to produce closed cells (and easterlies at central latitude).

We must stress that testing the dynamics against a multivariate red noise is much more constraining than using a univariate reference. In particular, V87 shows that no difference can be detected between the model and the red noise when studying the spatial decorrelation. The opposite result obtained by Gützler and Mo (1983), Horel (1985) and Dole and Gordon (1983) certainly accounts for the fact these authors use a univariate process as reference.

5. Persistence analysis

In this section we establish the main results of this study. Our aim is to show the existence of particular phase space and physical space locations where persistent anomalies tend to gather. Persistence analysis basically relies on fields comparison and requires a resemblance criterion in which an amount of subjectivity cannot be avoided. Different criterion are known to yield somewhat different results (Gutzler and Shukla 1984) and the analysis conducted below does not avoid this difficulty. However, a full discussion of the various choices is presented in V87. The red noise model designed in subsection (4d) is used as an objective reference for testing the adequacy of the method.

a. Persistence criterion and case selection

In the course of the present study, we started by using a similarity criterion between geopotential anomaly maps based on pattern correlation, as in Mo (1986). As Mo and Ghil (1987) point out, we noticed that so-defined persistent sequences generally correspond to high amplitude anomalies. The histograms of the streamfunction amplitude for selected persistent data then show a strong bimodality for longitudes located in the second quarter of the channel. But repeating the same experiment on the red noise data gave rise to a similar result though the process is by definition unimodal (see also appendix C). We have thus suspected that the correlation criterion systematically excludes small amplitude large-scale anomalies and one of our purposes has been to find a criterion which would be free of this bias.

An objective choice for persistence definition would give rise to a uniform distribution of persistence probability in phase space when the red noise data are analyzed. We are unable to derive such a criterion from pure mathematical considerations but it turns out, after several trials, that a criterion based on the rms of the difference between anomaly maps (as in Legras and Ghil 1985) is a suitable choice. It however tends to produce the reverse effect of the correlation criterion by favoring persistence around the mean flow. This bias somewhat penalizes the detection of persistent high amplitude anomalies. But if some cases are identified, their significance can only be reinforced.

Our study is based on the daily large-scale anomalies of the upper-layer streamfunction at the 32 grid points of latitude 7, as in section 4f, and for the sake of simplicity, we denote $\psi_i(t)$ ($i = 1, \cdots, 32$) the anomaly at longitude i and time t ($t = 1, \cdots, 45\,000$). We define a regional persistence score $s(t, T)$ of the se-

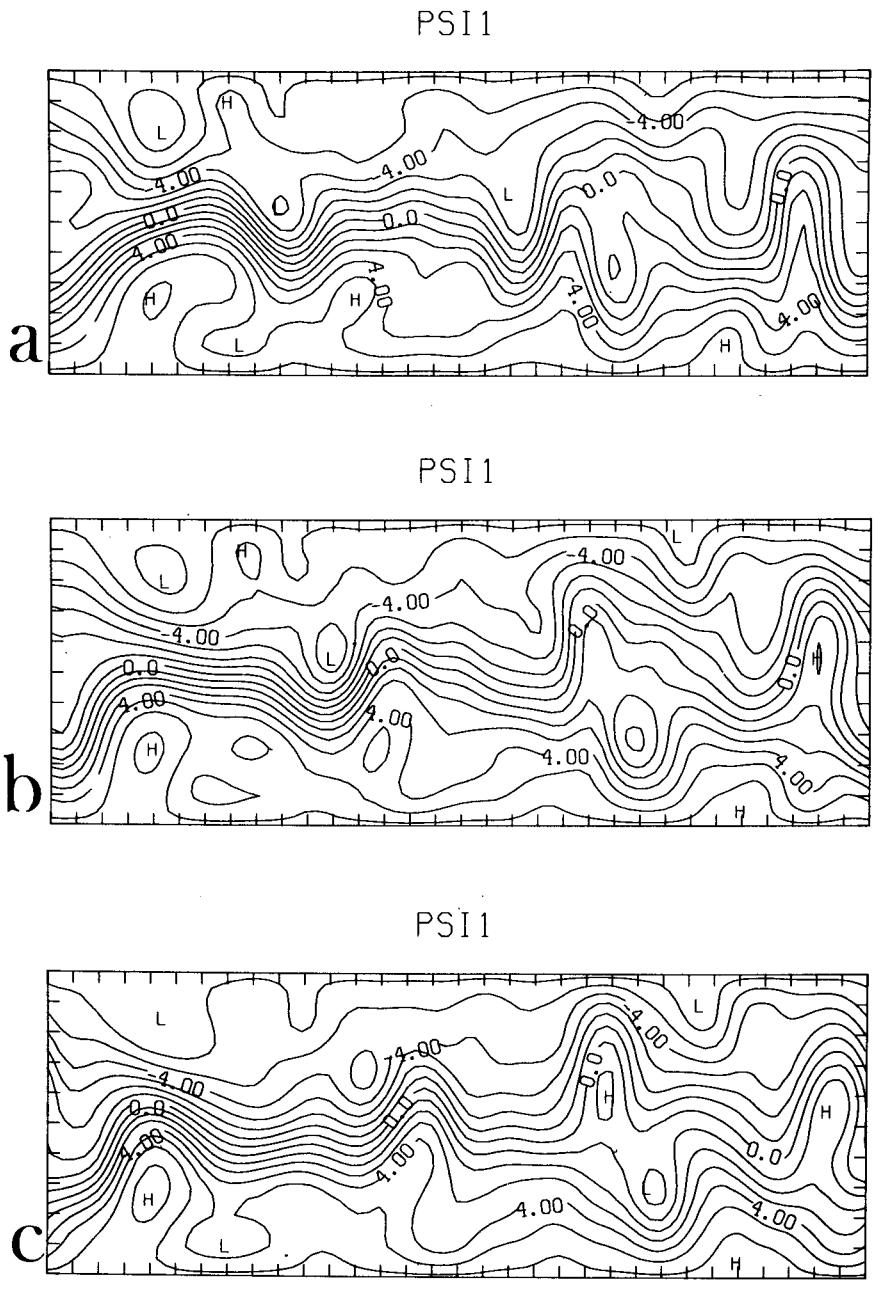

FIG. 13. (a, b, c) Sketches of a zonal period and (d, e, f) a blocking period. Contours show the upper-layer streamfunction for two series of three successive days. Units 10^7 m^2 s^{-1}.

quence of T successive days starting at day t in the following way: let N_1 and N_2 ($N_1 \leq N_2$) be the longitude bounds of a test domain, and let $\bar{\psi}_i(t)$ be the time average of ψ_i during this sequence. The regional amplitude $A(t')$ of the departure from $\bar{\psi}(t) = \{\bar{\psi}_i(t)\}$ at day t' ($t \leq t' \leq t + T$) can be measured by the spatial rms running over the test domain

$$A(t') = \left[\frac{1}{N_2 - N_1 + 1} \sum_{i=N_i}^{N_2} (\psi_i(t') - \bar{\psi}_i(t))^2\right]^{1/2}. \quad (5.1)$$

We then measure the regional persistence of the T-day sequence by looking at the maximum of $A(t')$ for t' running from t to $t + \tau$ and we define the *score* of the sequence as

$$s(t, T) = \max_{t \leq t' \leq t+T} (A(t')). \quad (5.2)$$

For large enough values of T (say larger than 10 days), high score is an indication of a break in the time-behavior during the sequence, and low score

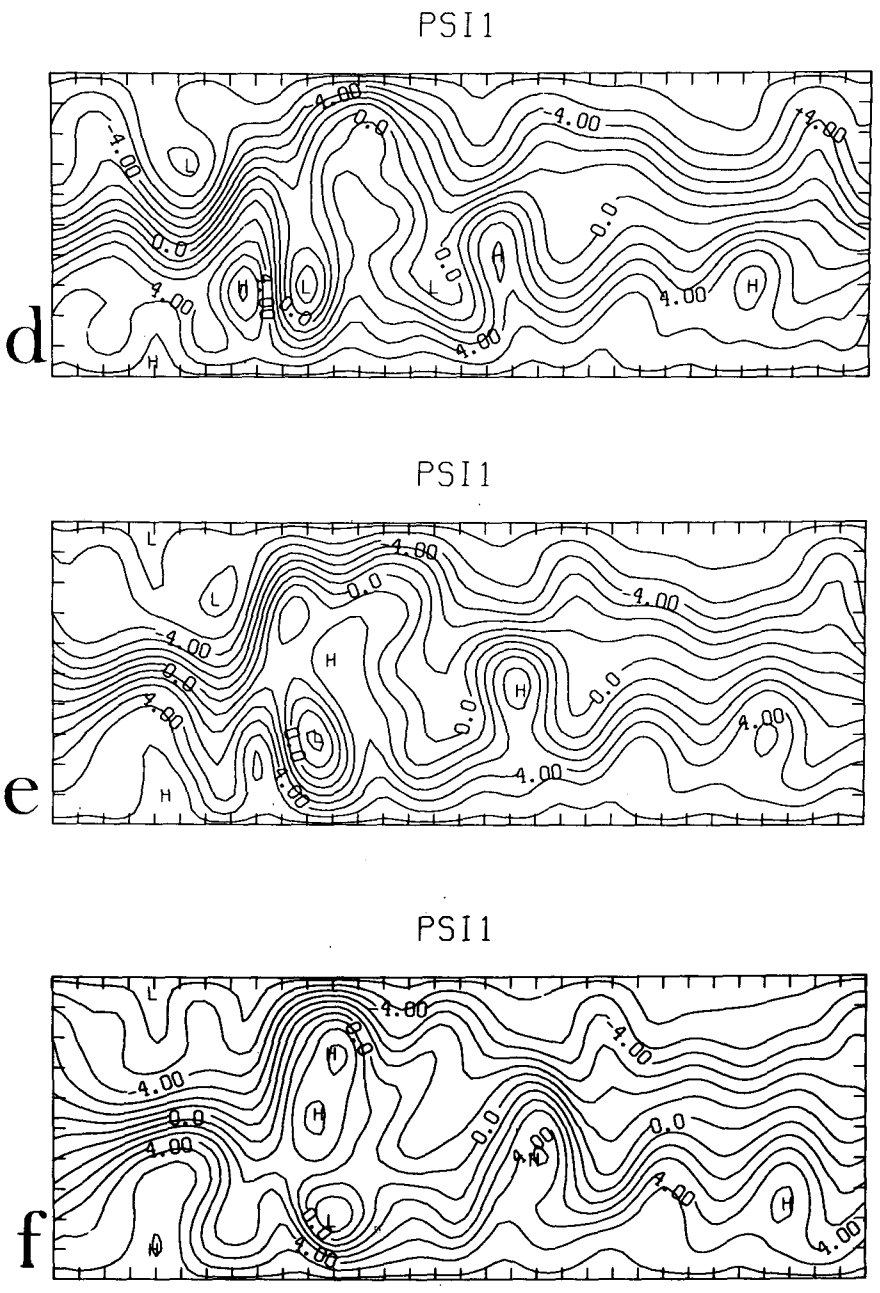

FIG. 13. (*Continued*)

characterizes a sequence during which the regional pattern does not dramatically change, even if the ambient noise is large. We fix $T = 15$ days according to the analysis of characteristic times presented in V87. We use the whole channel ($N_1 = 1$, $N_2 = 32$) as the area-of-field comparison. Vautard (1987) uses different areas and compares the results which, in turn, are significantly different. The comparisons show that using the whole channel at test domain eliminates the spurious effects met for the other possible choices, basically because the test domain is then much larger than the scale of the anomaly.

The first step of the analysis consists of selecting a subset of the original 45 000-day dataset that only contains persistent sequences. To this end, the 15-day sequences are sorted according to their scores $s(t, T)$ and the K most persistent sequences are retained where K is chosen so that one-third of the data is kept. Thus 15 000 days enter into the subset that we shall refer to as the *persistent dataset*. The maximum score $s_m = 5.6$

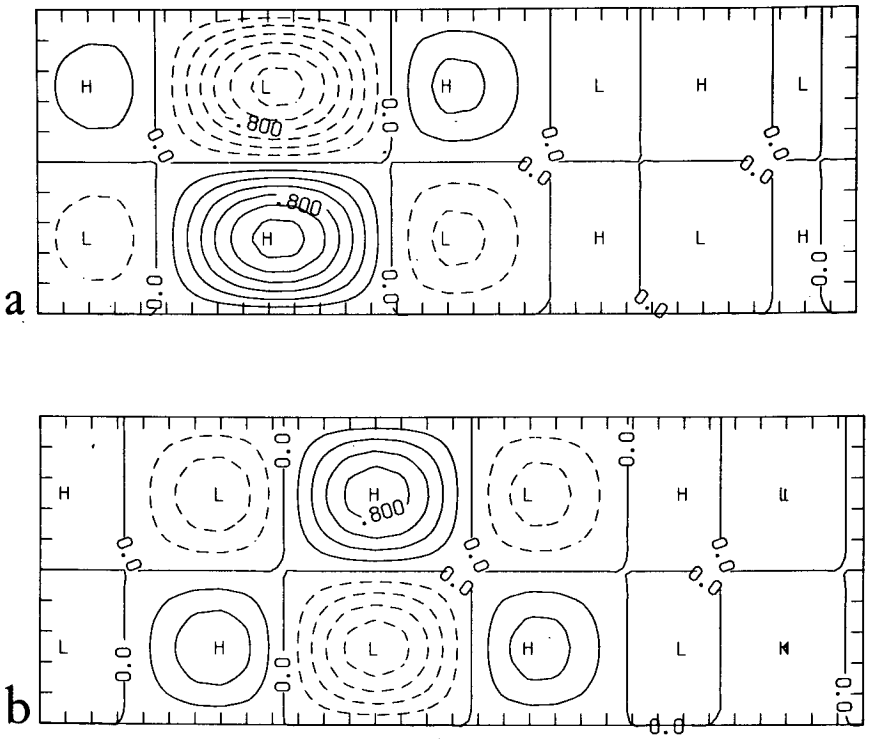

FIG. 14. Spatial pattern of the (a) first and (b) second EOF of the large-scale upper-level streamfunction computed over experiments A + B + C. Units 10^7 m^2 s^{-1}.

$\times 10^6$ m^2 s^{-1} (the Kth score in ascending order) can be interpreted as a threshold, corresponding to a uniform departure of 56 m of geopotential height. Since we are considering sequences and not individual days, there is a considerable overlap between adjacent periods, sometimes inducing a chaining between dramatically different patterns. We thus need a more accurate definition of *persistent cases.* A case is defined as a series of successive persistent 15-day sequences. For instance, if the 15-day sequences starting at days 1, 2, 6, 7, 8, 10 . . . are persistent, and sequences starting at days 3, 4, 5, 9 are not, a first case will run from day 1 to 16, and a second one from day 6 to day 22, etc. . . . Cases may still overlap, but during a given case, we expect that all the days exhibit the same anomaly pattern. This definition is used in (5c) for compositing particular persistent patterns. The procedure leads to about a total of 1000 cases, utilizing the 15 000 days of the persistent dataset.

b. *Geographical distribution of persistence*

We have already shown (cf. subsection 4d) that there exist some preferred geographical locations for the anomalies of the large-scale streamfunction in the upper layer. Now we want to see whether these anomalies are persistent or not. To accomplish this goal, the anomaly dates at each longitude i are computed, and the ratio

$$r(i) = \frac{\text{number of persistent anomaly days at } i}{\text{total number of anomaly days at } i} \quad (5.3)$$

is measured for each longitude. Here we use the weak amplitude threshold (50 m of geopotential height) to select the anomaly days and the persistent anomaly days are the ones among these latters that belong also to the persistent dataset. Figure 16 shows the ratio $r(i)$ as a function of longitude, for positive and negative anomalies, and for both model and red noise data. The significance is tested through a Monte-Carlo method detailed in appendix B. Ratios above (below) the confidence interval are significantly persistent (transient) for our test.

We immediately see that the red noise does not exhibit any significant persistence or transience for positive or negative anomalies. The model positive anomalies are persistent from longitude 12 to 18 and they are transient in the jet region and at the downstream end of the channel. At the very exit of the jet (longitudes 8–10), only negative anomalies are persistent, while they are significantly transient where positive anomalies are persistent. Thus, the asymmetry between positive and negative anomalies is emphasized when persistence is taken into account. From Figs. 15 and 16, we conclude that the preferred signs of relatively weak anomalies correspond to the preferred signs of persistent anomalies, and that persistent flows corresponding to

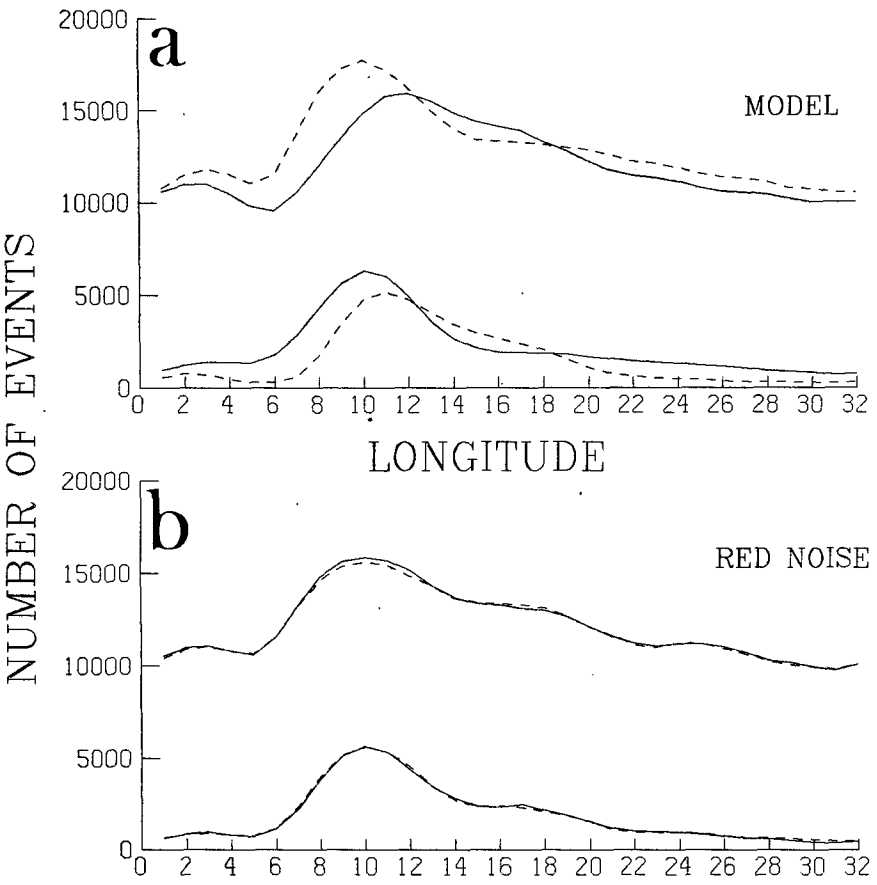

FIG. 15. Number of anomaly events as a function of longitude at latitude 7 for (a) the model data and (b) the red noise data for a threshold of 5×10^6 m^2 s^{-1} (upper graph of each figure) and a threshold of 15×10^6 m^2 s^{-1} (lower graph of each figure). Solid: positive anomalies. Dashed: negative anomalies.

weak anomalies can be classified into two kinds of patterns. The negative case is characterized by an extension of the jet and the positive case by a large diffluence of the flow near the center of the channel. For the much less frequent strong anomalies, similar results are obtained but they have low significance.

A related question is to see whether the persistent anomalies at given longitudes cluster around preferred values. We consider the probability distribution of normalized anomalies at longitude 6 (center of the jet) and 12 (end of the storm track). They are shown in Fig. 17 for the whole dataset and for the persistent dataset and for both model and red noise. The normalized anomaly λ is covered by 100 centered bins of width $\Delta\lambda = 0.6$ each and the densities m_i are estimated as

$$m_i = \frac{N(i)}{45\,000\Delta\lambda}, \qquad (5.4)$$

where $N(i)$ is the number of anomaly values falling within the ith bin. The corresponding number of degrees of freedom is ten. The 95% confidence interval is given by $m_i \pm 2\sigma(i)/10$, where $\sigma(i)$ is the density variance estimated from 100 samples of each set. The samples are formed by the partition of each set into 100 segments of successive data, each containing 450 days for the whole dataset and 150 days for the persistent dataset.

We see in Fig. 17 that a clear asymmetry is observed between positive and negative anomalies, as anticipated before. The distributions at longitudes 5 to 10 (not shown) exhibit the same positive skewness which is maximum at longitude 8, indicating a preference for the extension of the jet downstream from its mean location. At longitude 12, skewness is less pronounced but discrepancies occur between persistent distributions and the total distribution. The latter shows a rather flat top compared with red noise but there is here no indication of bimodality. This behavior is also supported from atmospheric observations (Dole and Gordon 1983) in the northeast Atlantic. On the other hand, Fig. 17d indicates the existence of preferred anomaly values for persistent days. The red noise does not reproduce this behavior, showing that our criteria is not biased in favor of bimodality.

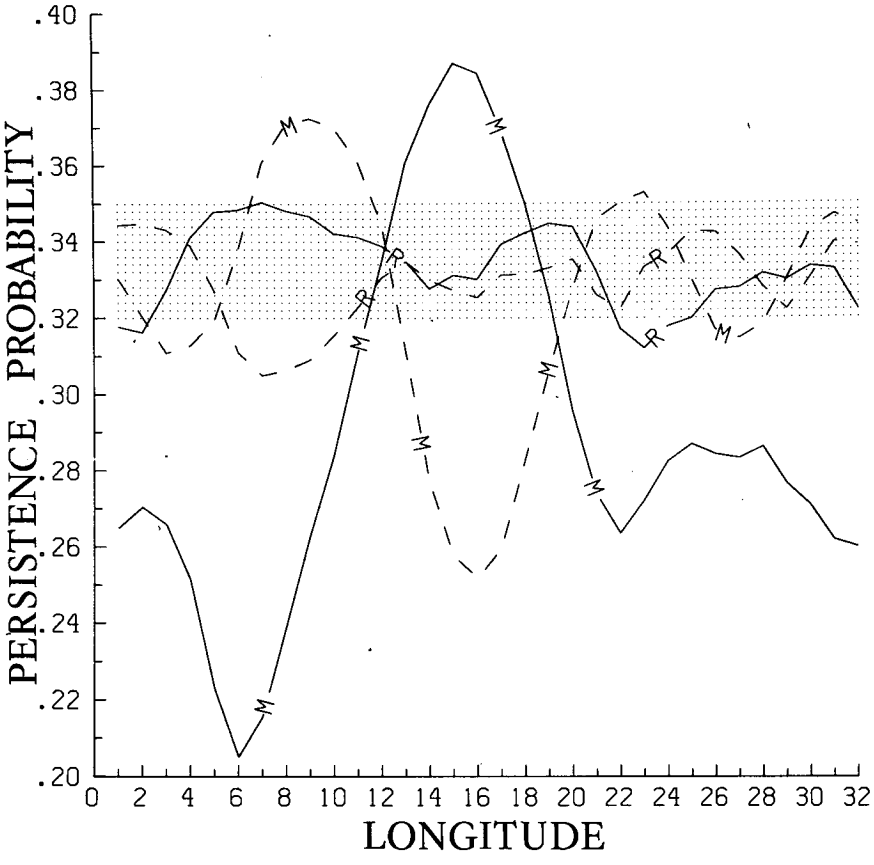

FIG. 16. Ratios $r(i)$ as a function of longitude i for positive anomalies (solid curves) of the upper-layer streamfunction exceeding 5×10^6 m^2 s^{-1}, and the corresponding negative ones (dashed lines) for both model (M) and red noise (R). The dotted region corresponds to the 90% confidence interval (see text and appendix B).

c. Distribution of persistence in phase space

Section 5b shows the need for a global approach to persistence properties and thus for a phase space investigation. For the sake of simplicity, we only consider the projection of the upper layer streamfunction onto the first two EOFs (shown in Fig. 14) which captures more than 50% of the large-scale variability. The time series of the associated PCs are centered and normalized by their standard deviations. Hereafter, we shall refer to them as $x_1(t)$ and $x_2(t)$. Figure 18 shows the histogram of the couples $[x_1(t), x_2(t)]$ for the whole 45 000 days. The histogram has been computed by counting the number of couples $[x_1, x_2]$ falling within 50×50 centered square boxes of size 0.6×0.6 running from -3 to 3 standard units in both directions. Note that positive values of x_1 mean negative anomalies at the very exit of the jet and positive values of x_2 mean downstream positive anomalies (longitudes 12–16). The distribution is skewed and it has, somewhat, the shape of a breached volcano, but does not show any trace of the bimodality reported in Hansen and Sutera (1986) for atmospheric flows. The red noise distribution (not shown) is well centered and displays circular contours since x_1 and x_2 are independent normal deviates.

The corresponding histogram for persistent model data (not shown here) has hints of similar properties though its shape is more elongated than for the total histogram, in agreement with subsection 5b. Thus, we see that a cursory examination fails to detect multiple regimes. However, it must be noted that if the persistence probability is uniformly distributed in phase space, the persistent histograms would exhibit exactly the same shape as the total histogram, since the probability of a given day belonging to a persistent dataset would be independent of the pattern on this day. Indeed, the main question is the dependence of persistence properties on the spatial pattern.

The *persistence probability* chart can be estimated by the ratio of the persistent histogram to the total histogram. Figure 19 shows the persistence probability for the two persistent sets, obtained from the model and the red noise data. Again, we use the same null hypothesis as in section 5b in order to test the significance. Points marked with the signs "+" ("−") delim-

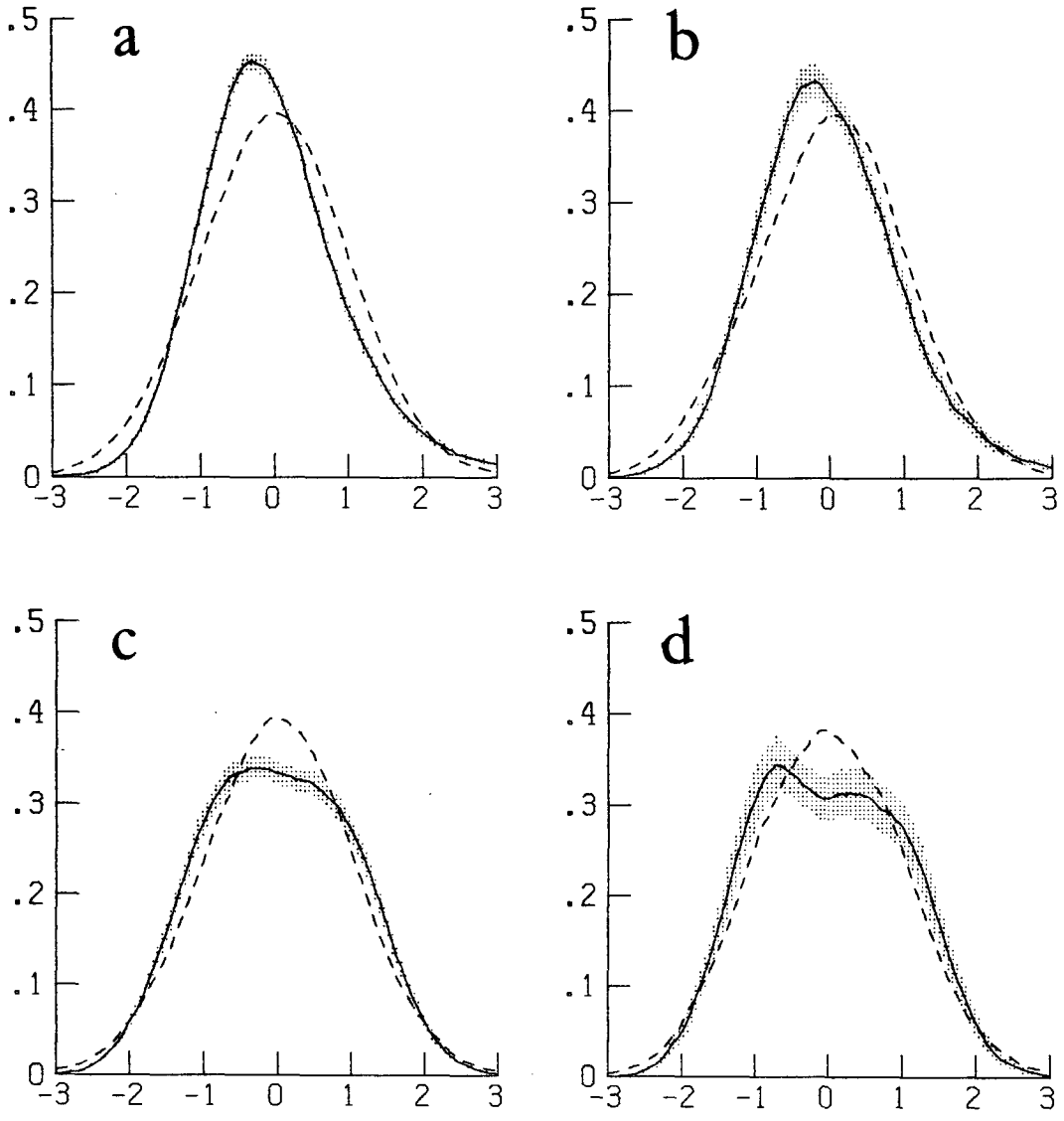

FIG. 17. Probability density distribution of normalized anomaly at longitude 6 for (a) all data, and (b) persistent data. Panels (c) and (d): the same as (a) and (b), respectively, at longitude 12. In each diagram, the dashed curve is plotted with the red noise data. Dotted region: confidence interval for the distribution (see text).

itate the domains wherein the persistence probability is larger (lower) than that obtained with a *random definition of persistence*, (appendix B) with 5% chances of being wrong. The probability shows two maxima corresponding to two distinct regions of phase space. However a larger region of significantly high probability covers the interval between the two maxima, which are therefore not well separated. High values of x_2 and low values of x_1 are preferred, corresponding to high positive anomalies in the second quarter of the channel.

As anticipated in section 5b, the persistence criterion when applied to the red noise selects preferred patterns resembling the average, whereas for the model data this region is close to the domain of significant transience. In addition, red noise distributions exhibit, as expected, good symmetry with respect to the mean flow.

We may conclude that persistence properties are inhomogeneously distributed in phase space, but persistence does not occur within sharp regions, and no special pattern seems to be systematically persistent. (Values larger than 0.48 are never reached.) On the other hand, our criterion underestimates the separation between persistence domains since, according to our discussion in section 5b, we are far from the perfect definition of persistence that would not favor any phase space region for red noise. We have also tested the same procedure with a criterion based on correlation and

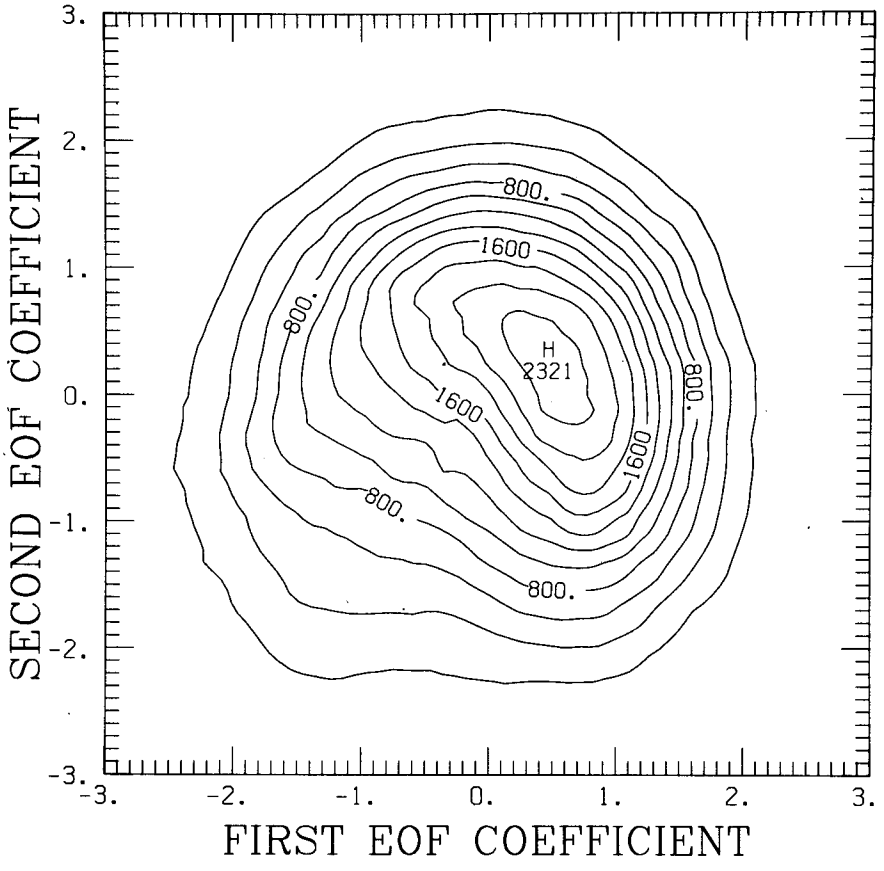

FIG. 18. Histogram of the couples $(x_1(t), x_2(t))$ for the whole model dataset.

we show in appendix C how big the opposite effect is, i.e., the rejection of measured persistence from the vicinity of the red noise average.

Other probability calculations were also performed using different sequence lengths, $T = 5$, 10, and 20 days for the selection of cases. For $T = 5$ days the persistence criterion does not produce separation of regions, because sequences with smooth trend are also detected as persistent sequences. For $T = 10$ and 20 days, the same results as for $T = 15$ days hold, and the separation properties are improved with $T = 20$ days. Beyond this limit, persistent data gather in cases that are too long, and their independence is thus largely affected.

d. Zonal and blocking flow

The aim of this subsection is to study the characters of preferred persistent patterns. We select the cases (see section 5b for definition) for which at least one element falls within one of the two boxes plotted on Fig. 19a over the two peaks of the distribution. The data from each subset are then gathered within *periods* which do not overlap. Here, 160 periods containing 3275 days were selected using the lower right box and 64 others containing 1227 were selected using the upper left box. They are called, respectively, zonal and block periods.

Figure 20 shows the composite of the large-scale circulation over zonal periods. Compared to the mean flow shown in Fig. 6, this circulation exhibits a reinforced zonal flow within a considerable downstream extension in both layers. There exist only weak oscillations elsewhere in the channel and we see that the vertical tilt observed for the mean flow is still present here. Figure 21 shows the composite of the large-scale circulation over the block periods. The associated pattern exhibits a marked diffluence of the jet within the second quarter, and a well-defined dipolar structure centered at longitude 12 in the upper layer where weak easterlies occur at central latitude. The same pattern is reproduced in the lower layer, and we see that the vertical phase tilt is almost negligible. It is noteworthy that even if we perform a selection of persistent cases based on upper-layer flow only, intense anomalies are preserved within the lower layer.

Figure 13 is built from two persistent sequences belonging to zonal and block periods. The splitting of the transient eddies observed during the block sequences is confirmed in Fig. 22b which shows the variance of ψ_1 over the block subset. It is clearly seen that

eddies weaken considerably during their propagation around the block. This variation of the storm path is in good agreement with the observational study of Dole (1985). Conversely, the variance during zonal periods, Fig. 22a, exhibits a well-marked storm track structure extending well downstream from the mean jet region. This indicates two different interaction mechanisms during zonal and blocking sequences. In the first case, the eddies do not weaken as they cross the anomaly, but downstream. Thus, the positive feedback of transient eddies cannot be the main factor in maintaining the anomaly for zonal periods. In the second case, the eddies rapidly weaken within the anomaly domain and the positive feedback is more likely to play a key role. This possibility is confirmed by Fig. 23 which shows the eddy potential vorticity fluxes and their convergence, in the same representation as in Fig. 9 in both cases. Within the jet region, vorticity fluxes exhibit a similar pattern in both cases, whereas downstream they tend to circulate around the elongated storm track of the zonal case and the split storm track of the block case. Comparison with Figs. 20 and 21 shows that the transients have a positive effect on the corresponding large-scale flows, except at the upstream end of the jet where they tend to decelerate the zonal wind. In particular, Fig. 23b shows a clear contribution to the reinforcement of the blocking pattern. Comparatively, the acceleration of the zonal wind is rather weak within the anomaly region in the zonal case confirming the reduced ability of eddies to maintain the extended jet than to maintain the blocking pattern.

In addition, V87 studied the intraperiod and the interperiod variations for both regimes. He found in the zonal case that the intraperiod variance is rather homogeneous over the whole channel but is weaker than the interperiod variance showing that the zonal anomaly pattern is not well defined. Conversely, in the blocking case, the two types of variance are of similar amplitude and the phase fluctuation of blocking anomalies can be linked with the fluctuations in eddy activity.

6. Parameter sensitivity

Thus far, the parameter set used is derived in section 2 from realistic atmospheric values. However, the model itself depends on rather crude approximations, and the parameters are defined with large uncertainty within the so called realistic range. We thus need to estimate the sensitivity of our results to variations of the main parameters. Since it would be too costly to perform many 15 000-day integrations, we only consider 5000-day samples. As a preliminary, we have to test whether a 5000-day sample is able to provide sufficiently significant results. Beyond the saving of computational cost, this question is also of practical importance for future work because the available atmospheric records do not extend over 15 000 days for a given season but rather over durations of 4000 days and less.

a. Reduced sampling of the basic experiment

We divide the 45 000-day dataset, taken as a reference, into nine consecutive 5000-day subsets. We find that the variance and flux maps are essentially unchanged, indicating that 5000 days are enough to compute first- and second-order moments. On the other hand, there is a noticeable variability between persistence estimates.

The persistence criterion is applied independently to each of the nine samples, now selecting 2000 days among the 5000, but still using the same sequence length $T = 15$ days and the two-dimensional persistent histograms are calculated using the same method as in section 5c. They visually differ from one to another; in particular, seven of them exhibit a clear bimodality but the locations of the peaks vary a lot from one sample to another.

The persistence probability is thus computed for each sample, and the significance is estimated by using, for each of the nine estimations, a different set of 100 test subsamples, as in Appendix B. In order to check the quality of the test, we have counted for each (x_1, x_2) box the number of 5000-day samples giving a probability significantly larger (smaller) than for the random definition of persistence given in Appendix B. For a given box, if at least one estimate is significantly large and another significantly small, we conclude that the significance test gives unreliable information. Only 3% of the boxes fall into this category. Since the confidence level is estimated at 95%, we may say that the test is a good estimate of the significance for the variable which takes only the two values "above" or "below" the random persistence bounds.

In addition, the unreliable boxes are located near the boundaries of significant regions. Near the peaks of the probability distribution shown in Fig. 19a no box is found to be in the unreliable case. Indeed all the probability estimates at least show two significant maxima, the locations of which vary with the sample but nevertheless fall within the domain of significant persistence of Fig. 19a. We conclude that 5000 days are sufficient to estimate whether persistence regions scatter within phase space but the detailed features require more information to be correctly estimated.

b. Sensitivity to the mean wind

We describe three experiments performed with the parameters given in section 2, for three different values of the mean wind $U = \frac{1}{2}(U_1 + U_2)$, chosen in such a way that the mean shear $DU = U_1 - U_2$ is unchanged. We respectively fix the values $U = 10$, 14 and 16 m s^{-1} in the three experiments denoted as U1, U2 and U3. From Table 1, we see that the e-folding time of the most unstable mode does not change while its period decreases with increasing zonal wind, as expected.

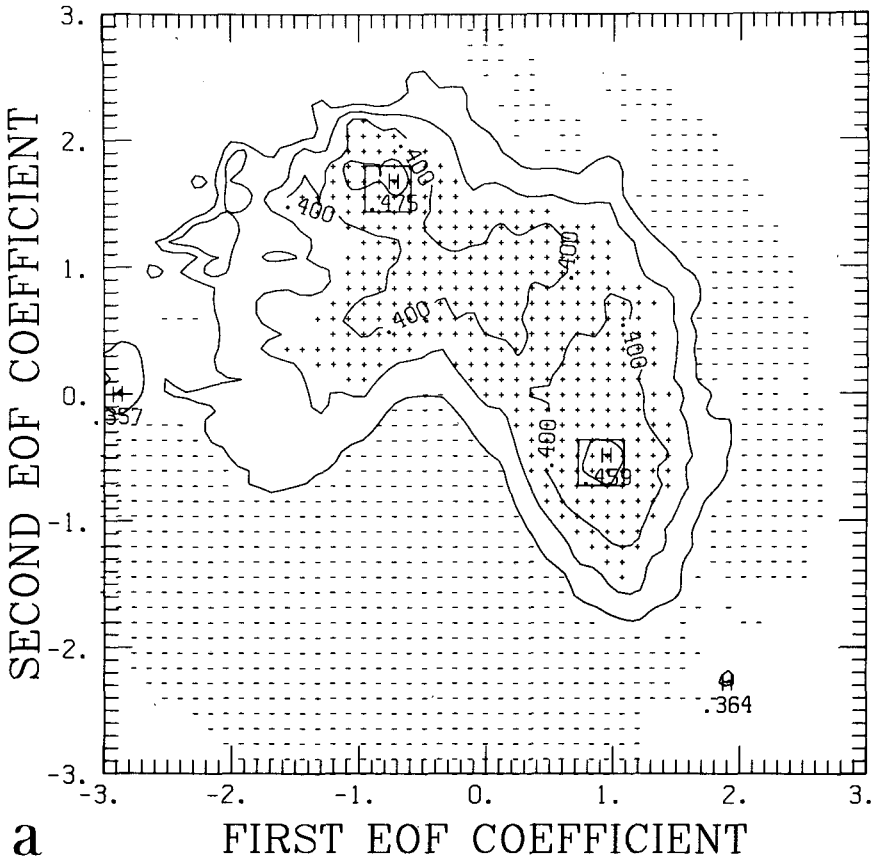

FIG. 19. Persistence probability as a function of x_1 and x_2, for (a) model and (b) red noise. Signs "+" ("−") denote boxes of significant persistence (transience). Square boxes are placed on the maxima of (a), used for composites selection (see section 5e). Contours run from 0.30 up to 1 with interval 0.05.

The local unstable stationary eigenmode discussed in section 3 exists in the three cases and is only slightly deformed by the different zonal advections. It however undergoes large variations of its e-folding time τ_b.

Figure 24 shows the variance maps of nonfiltered eddies for experiments U1, U2 and U3. They must be compared with Fig. 7. In U1 and U2, no dramatic change appears compared with the basic experiment, except that the diffluence is shifted downstream in U2 and upstream in U1. On the other hand, no clear diffluence pattern occurs in U3. In the three experiments, the central maximum of the variance is not displaced and, moreover, the small-scale variance (not shown) does not vary either in shape or in amplitude, indicating that the small-scale activity is rather insensitive to the mean wind. The variation of total variance is entirely due to the change in the large-scale component. In U3, the large-scale variance is not confined within a sharp region but extends from the jet exit to the center of the channel, with less well-defined maxima. These results indicate a change in large-scale behavior when the zonal wind exceeds 15 m s^{-1}, whereas in U1 and U2, the behavior is essentially the same as for the basic experiment but accompanied by a phase displacements of the large-scale structures. The visual inspection of daily fields in U1 and U2 still shows the alternation of zonal and blocking regimes. Conversely, anomalies are less local and less persistent in U3. The large-scale EOFs are calculated as in section 4d. Table 1 contains the variances associated with the first two EOFs and the corresponding fraction of the total variance. In all cases, the patterns resemble the patterns of Fig. 14, so that the variances can be easily compared. Although the total variance slightly increases with U, the variance explained by the first EOF decreases, and in U3, the EOF_1 and EOF_2 variances are of the same order confirming the phase fluctuation of large-scale patterns.

The persistence analysis is performed in the three experiments, selecting 2000 persistent days among the 5000-day datasets. Although the persistence probability maps are not highly significant, as mentioned previously, they show clear differences between the U1, U2 and U3 experiments. In U1 and U2, the distribution of persistence is split into two regions located near the

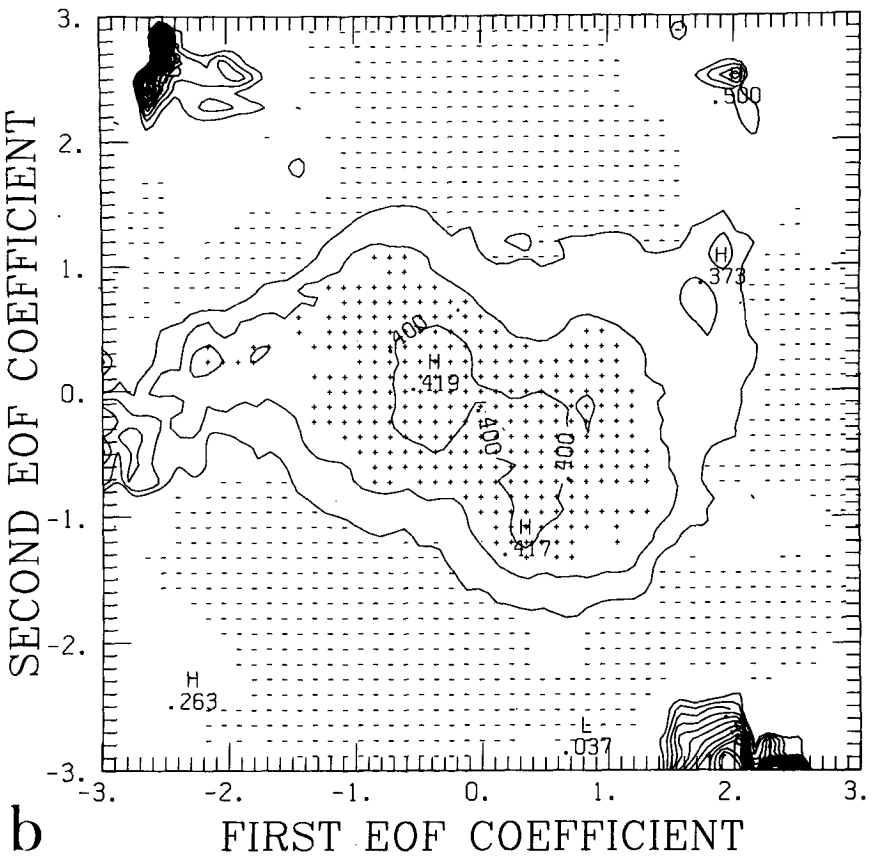

b

FIG. 19. (*Continued*)

maxima of Fig. 19a whereas in U3, the persistent states are near the mean flow and no bimodal distribution of persistence is observed.

We may understand these results in the following way: The location at which baroclinic perturbations reach their mature stage, and thus the regions where the large scales are forced by nonlinear feedback, is determined by the mean wind advection. The larger the mean wind, the further downstream from the jet maximum the location of large-scale response. This accounts for the variations observed between U1, U2 and the basic experiment. On the other hand, phase locking requires that the large scales are not too far from the linear stationarity condition. This condition is largely dependent on the mean wind: for instance, in the homogeneous case, the period of the mode (3, 2) is 53 and 56 days in U1 and U2, respectively, but drops down to 27 days for U3. One may thus expect that for sufficiently strong zonal wind, a break of phase locking occurs and the large-scale response is no longer local.

c. *Variations of the mean shear*

Two experiments are performed with $DU = 10$ and 14 m s^{-1}, denoted as DU1 and DU2, with the same mean wind value as in the basic study, namely $U = 12$ m s^{-1}. Table 1 shows that the period of the most unstable mode does not vary significantly, while its *e*-folding time is greatly affected.

The variance of the streamfunction is found to be very dependent on DU. In DU1, Fig. 25a, it exhibits only a storm-track structure without any diffluence, and can be shown to be essentially due to small-scale eddies. In this case, transient forcing is not strong enough to force large-scale structures. One may add that in DU1, the variance map closely resembles the phase-averaged variance of the most unstable mode, indicating that the behavior is quasi-linear. On the other hand, in DU2, Fig. 25b, the variance exhibits the same pattern as in the basic experiment, but the amplitude is roughly doubled. Visual inspections of the daily fields show that in this case large anomalies of the streamfunction often occur and produce an alternation of strong blocks and strong zonal circulations. The model is thus found to be very sensitive to variations of the mean shear. This sensitivity is well represented in Table 1 by the variance of the first two EOFs. It can be readily seen that the large-scale response to the mean shear is very large in DU2. As in the basic experiment, the persistence probability for DU2

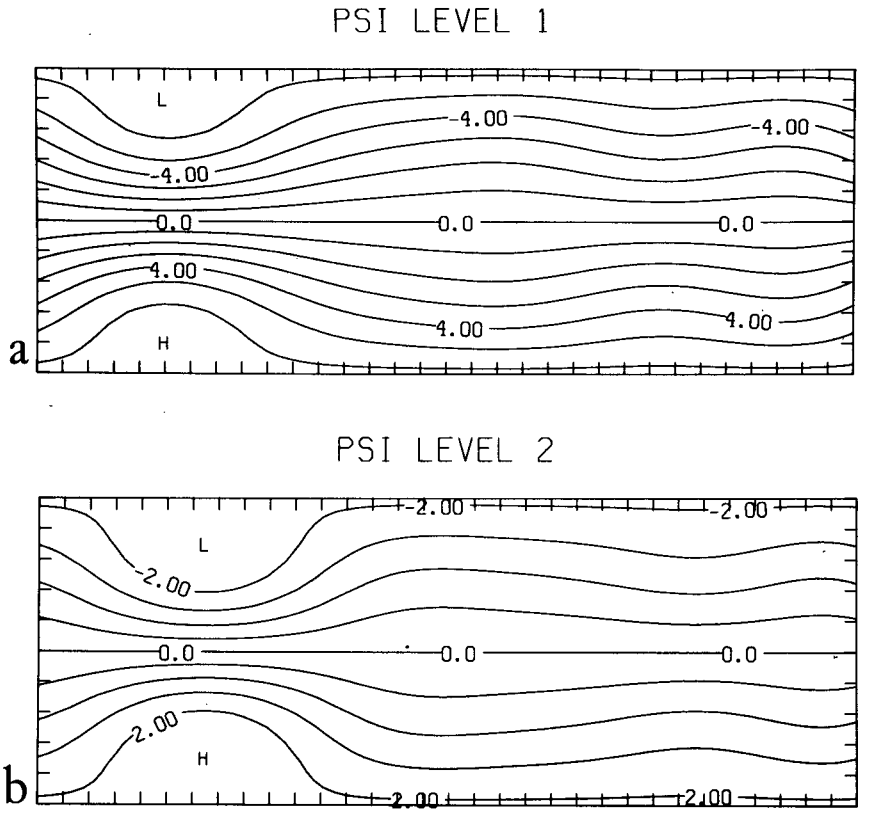

FIG. 20. Streamfunction composite of the zonal periods. (a) Upper layer, and (b) lower layer.

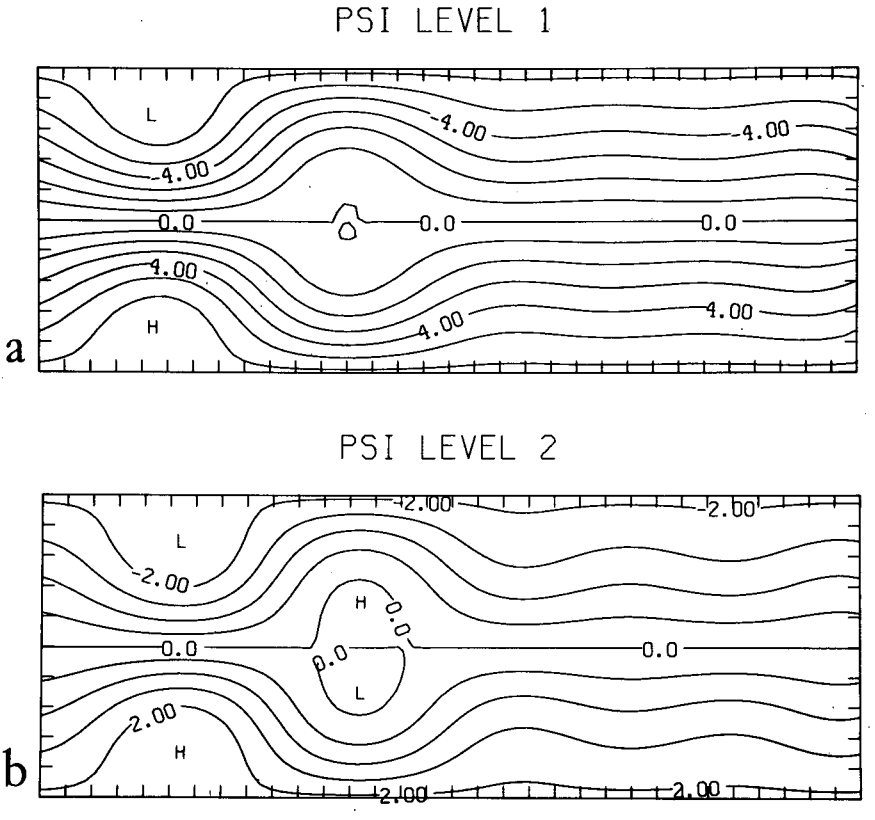

FIG. 21. As in Fig. 20 except for block periods.

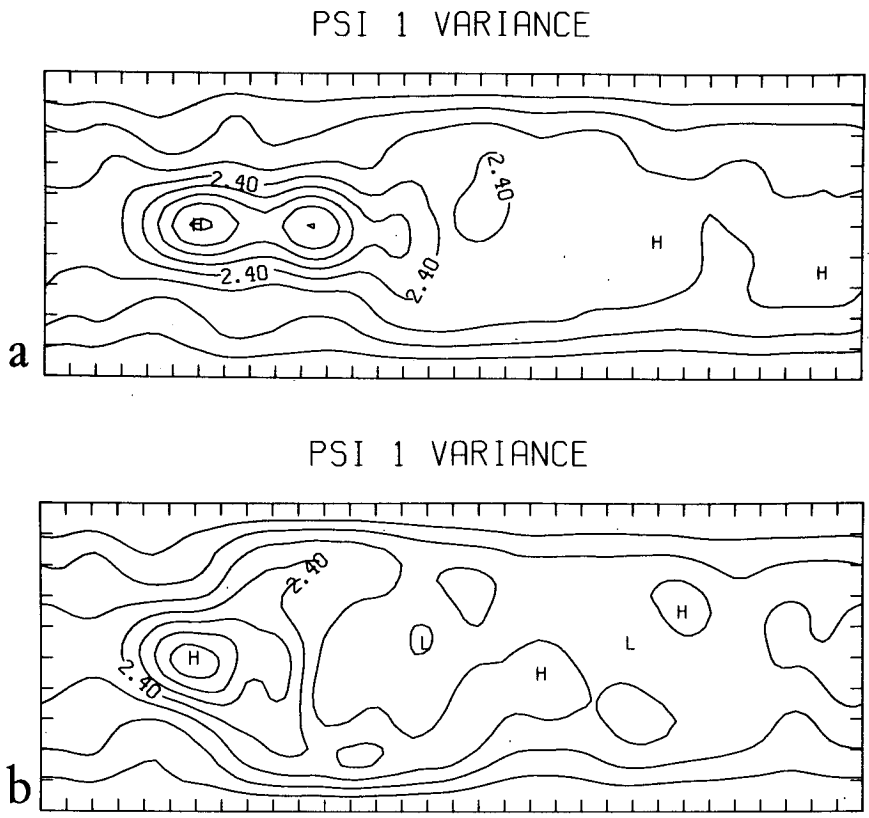

FIG. 22. Variance of the upper-layer streamfunction within (a) zonal subset and (b) block subset. Units 10^{14} m^4 s^{-2}. Contour interval 0.6×10^{14} m^4 s^{-2}.

spreads out over a large elongated region in phase space. In DU1, persistent patterns concentrate near the mean flow.

d. *Variations of local forcing amplitude*

We perform a 5000-day experiment (F1) with all the same parameters as for the basic case, except for A^* (see section 2) which is reduced in such a way that the maximum shear at the center of the basic jet becomes 27 m s^{-1}. For this new basic flow configuration (ψ_1^*, ψ_2^*), periods and e-folding times of baroclinic instabilities are only slightly modified, whereas no local stationary unstable eigenmode exists, cf. Table 1. Figure 26 shows that the total variance is largely reduced by the decrease of inhomogeneity amplitude. However, the variance keeps a diffluent shape at the exit of jet. Large-scale and small-scale variance are of the same order in magnitude and their maxima are located in the same places as in the basic experiment. The reduction of the variance is also seen in Table 1 for the first and second PCs. Again, the first two EOFs display the same qualitative patterns as for the basic experiment. The low-pass variance is also associated with the alternation between blocking and zonal episodes, although the anomaly amplitudes are weaker and closed-cell blocks appear relatively rarely. The persistence probability is as scattered as in Fig. 19a with again two significant maxima. Clearly, a variation of the inhomogeneity amplitude does not dramatically change the nonlinear behavior of the model. The model is less sensitive to this forcing than to the mean shear.

One sees that the existence of intermittency in the large-scale behavior depends crucially on the imposed mean shear, and the inhomogeneity actually acts to fix the locations of high amplitude anomalies. Thus, the major part of the available potential energy extracted by the baroclinic eddies comes from the global average shear. We imply, in contradiction to Pierrehumbert (1984), that the local source of baroclinic instability does not fix the growth rate of the perturbations. Still, it fixes the location of the storm track and thus the location of the intermittent response of large-scale coherent structures.

7. Summary and concluding remarks

In order to investigate the relation of transient feedback with the midlatitude low-frequency variability, we have built a minimal model, consisting of a quasi-geostrophic two-layer channel forced by a local baroclinic jet superimposed to a constant uniform shear.

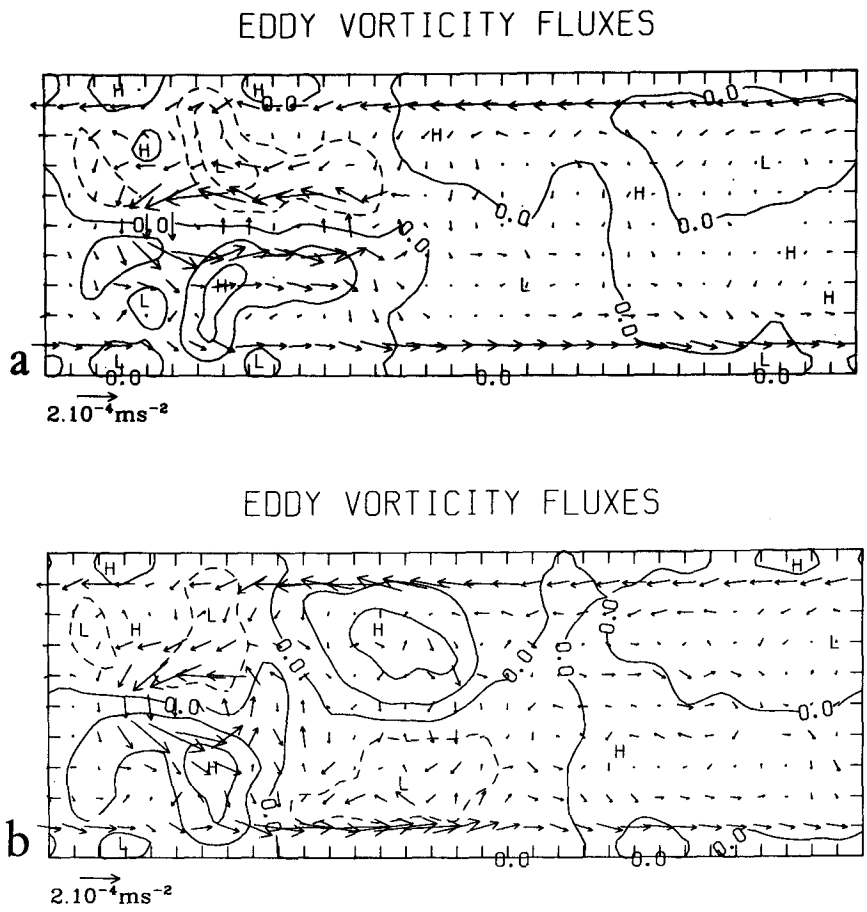

FIG. 23. As in Fig. 9 except for (a) zonal subset and (b) block subset.

Unlike some previous studies, all parameters are based upon reasonable physical assumptions.

Herein, in Part I of our study, the model is diagnosed by a series of methods which, when combined together, yield a clear picture of the dynamical properties. Beginning with the eigenvalue problem of the model linearized around its basic state, we show that the main effect of the zonal inhomogeneity is to concentrate near the exit of the jet the baroclinic activity of the most unstable modes. We also show that a modulation of the jet can be excited by the nonlinear feedback of the most unstable mode onto a slightly unstable localized stationary mode. The analysis of the average flow from a long integration of the model reveals that this mechanism actually saturates and explains the observed difference between the average flow and the basic state.

Space–time spectral analysis shows that the variability separates into large-scale quasi-stationary structures and small-scale high-frequency traveling disturbances. The small-scale component of the total vari-

TABLE 1. Characteristics of the sensitivity experiments, and of the basic experiment (R). The J_1, J_2: adimensional variances of the CP1 and CP2 coefficients (normalized by 625×10^{-11} m^4 s^{-2}). Here r^1 and r^2 are the associated percentages of the total variance, τ and T are the e-folding time and period of the most unstable mode, and τ_b is the e-folding time of the stationary local mode.

	σ_1	σ_2	r_1	r_2	τ	T	τ_b
U1	13.5	7.0	35%	18%	3.6	7.4	26.7
U2	11.6	8.1	29%	20%	3.5	4.5	10.4
U3	10.7	8.6	24%	19%	3.5	3.8	22.9
DU1	3.2	2.7	29%	25%	5.4	5.4	7.9
DU2	23.1	14.6	28%	17%			
F1	6.7	4.6	27%	18%	3.8	6.0	
R	12.2	7.5	32%	19%	3.5	5.6	11.1

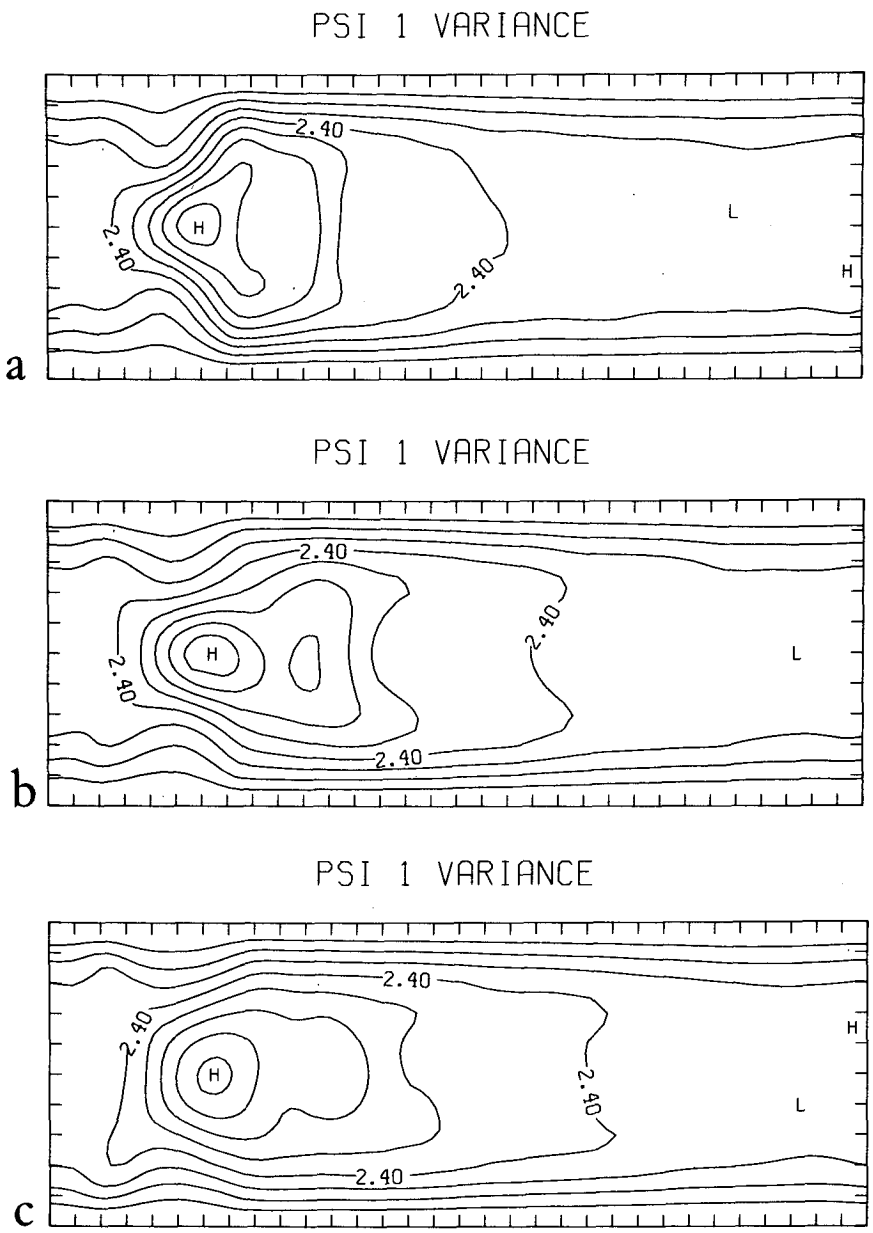

FIG. 24. Total variance of the streamfunction averaged over experiments (a) U1, (b) U2, and (c) U3. Units 10^{14} m^4 s^{-2}. Contour interval: 0.6×10^{14} m^4 s^{-2}.

ance exhibits a storm-track structure extending downstream from the jet maximum while the large-scale component is maximum off the center of the channel near to the end of the storm-track. Complex principal component analysis captures the storm-track structure but shows that local wavenumbers and frequencies are smaller than their counterpart given by the most unstable mode of the basic flow.

In order to provide a stochastic reference, a multivariate auto-regressive model was built so that it possesses the same covariance and cross-correlation at 1-day lag as the original model. The red noise is used to assess the existence of preferred locations for positive and negative anomalies. We also show that there is a tendency for long persistent sequences (beyond 15 days) to be associated with high amplitude large-scale anomalies.

A systematic study of persistence is conducted using a criterion based on rms of the streamfunction variations during test periods of 15 days. The persistent anomalies at a given longitude exhibit a generally skewed distribution. However, the two-dimensional histograms of the first two principal components do not show any bimodality, for both total and persistent

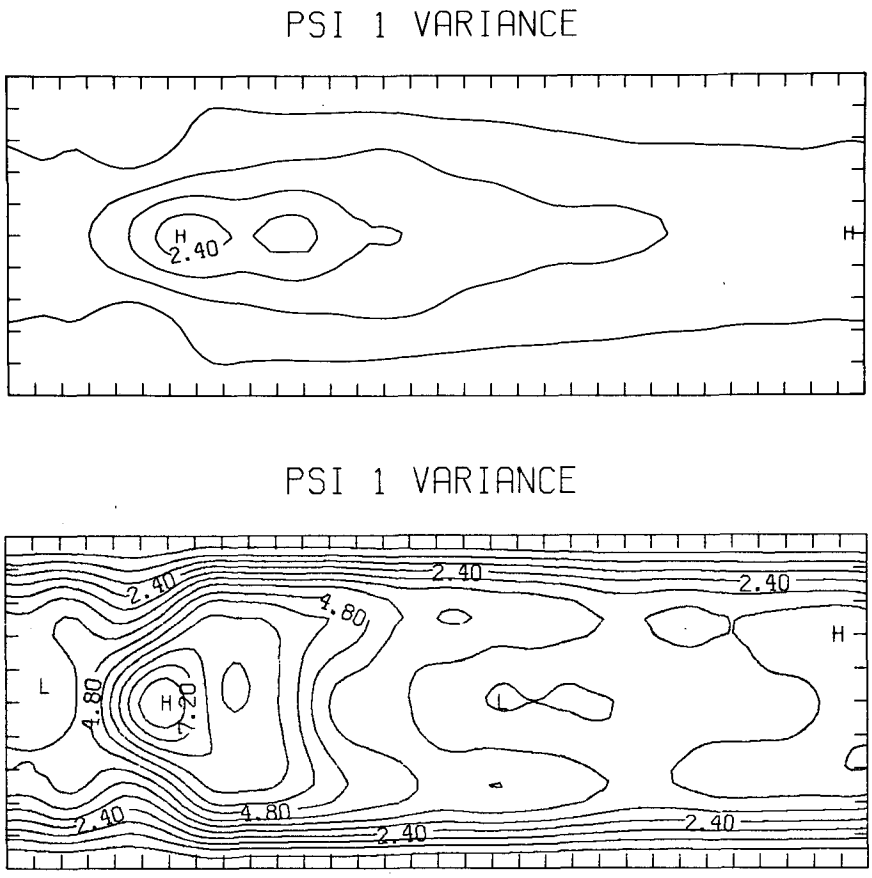

FIG. 25. As in Fig. 24 except for experiments (a) DU1, and (b) DU2.

data. Still they are highly non-Gaussian, with concentrations along a curved crest around the average flow. The dynamical relevant quantity is indeed the probability of persistence (for a given flow regime) which shows a very inhomogeneous distribution in phase-space and several separated maxima. The two composites based on the two main maxima correspond to two different regimes, of zonal and blocking type behavior, respectively. The transient feedbacks, computed in both cases, have a positive role in extending the jet

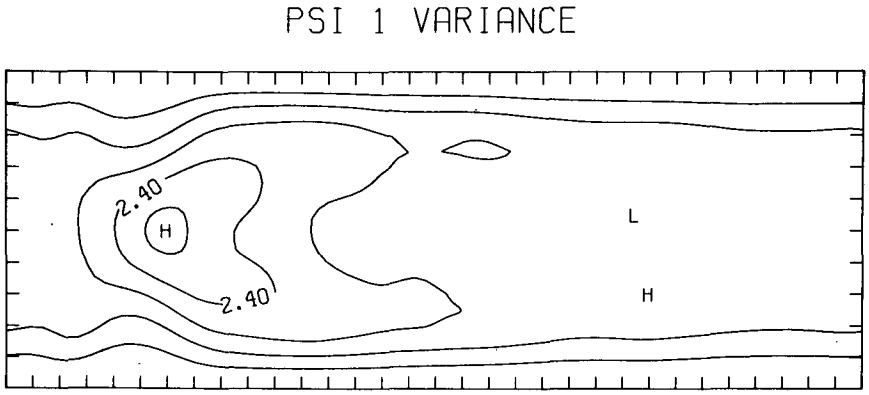

FIG. 26. As in Fig. 24 except for experiment F1.

downstream but the primary activity is in the maintenance of the dipolar structure located downstream from the jet in the blocking case.

The main result of this study is that a localized source of baroclinity in a very simple model induces behavior which bears numerous similarities, both qualitatively and quantitatively, to the observed atmospheric dynamics. The structure composed by the jet, the storm track of synoptic perturbations and the center of low-frequency activity, are studied in great detail and it is shown that several regimes are preferred in terms of persistence properties, although they do not occur sufficiently often to be directly visible from geopotential histograms. The transient feedback plays a positive role in the maintenance of the low-frequency anomalies.

Our model is, however, a very crude approximation of the real atmosphere, and we do not believe that it would be sensible to carry on further comparisons. However, it would be very interesting to investigate whether the persistence properties of atmospheric flows resemble the model behavior, as these features give a possibility of improving the extended weather forecast. A limitation of our approach is the requirement of a large dataset in order to obtain statistical significance for the measured quantities. Unless we are patient enough to wait a few decades, the atmospheric data will hardly give satisfaction in this regard. But state-of-the-art GCMs can fill the gap and long integrations will soon be available to allow very precise measurements of probability distributions. A very limited use of the dynamical information is done at the analysis stage of our study; we do not use the fact that the field is a geopotential field and that we know rather well (indeed, exactly for our model.) the rules of its evolution. Part 2 of this study (Vautard and Legras 1988) develops a dynamical-statistical approach that partly completes this problem.

We emphasize in this study the comparison between our deterministic model and a reference auto-regressive process. The choice of this latter is arbitrary and represents the crudest stochastic approximation to the investigated dynamics. We have, however, shown the importance of the inclusion of more than one degree of freedom within a stochastic representation simulating atmospheric data. Based on our study, more sophisticated stochastic models can be built that account for a larger part of the observed behavior and approximate, in a better way, the invariant measure of the large-scale attractor. The present study is only one step in this direction.

Acknowledgments. We particularly thank Michael Ghil for valuable discussions and communication of several references and unpublished results. We benefited of numerous useful comments from Brian Reinhold on the first version of this article. The manuscript was typed by Marie-Christine Cally. The computer resources were allocated by the Scientific Council of the Centre de Calcul Vectoriel pour la Recherche. Figures were plotted by the NCAR Graphics Software.

APPENDIX A

Lateral Boundary Conditions and the Conservation of Invariants

Expansion (2.4) uses lateral sine modes for both zonal ($n = 0$) and nonzonal components ($n \neq 0$). It is known (e.g., Vallis 1985) that this choice does not lead to the automatic conservation of the total vorticity in each layer in inviscid conditions (or equivalently does not verify the Phillips boundary condition). An expansion of the zonal components into cosine lateral modes cures this deficiency. However, our choice allows automatic conservation of the total momentum which is lost in the cosine expansion, and is technically very advantageous because it allows fast Fourier transforms in both directions without the need of costly projection of sines over cosines (as used by Vallis 1985). We must stress that the difficulty arises only as a consequence of the finite truncation of the expansion of 2.4 since the original equation, 2.2, conserves both invariants. In one case (sine expansion) an individual zonal mode does not carry any mean momentum but may possess a mean vorticity, while it is the opposite in the other case (cosine expansion). Thus a finite truncation of the spectral representation does not allow simultaneous conservation of the mean momentum and the average vorticity in the unforced and inviscid case. The problem may be serious at very low truncation but the discrepancy vanishes as $1/M$ when the resolution increases. Using several truncations, we found that the violation of the Phillips condition with $M = 13$ is of the same order as the fluctuations of the smallest scales and is anyway smaller than forcing and dissipation when incorporated. However, we must remark that our formulation introduces an additional constraint since the flow must possess zero vorticity at lateral boundaries.

APPENDIX B

A Random Reference for the Persistence Analysis

We need to test the estimated probability of persistence against the null hypothesis that it does not differ from what arises from a random definition of persistence. The latter is a layman's hypothesis but nevertheless requires careful definition. Choosing, for instance, 15 000 days at random among the 45 000 archived can be blamed to give us a definite advantage since we then neglect the important gathering of days within the persistent dataset which dramatically reduces the number of degrees of freedom. A more reasonable choice is to consider the 45 000 days as composed by a succession of transient periods of lengths $[n_j]$ and

persistent periods of lengths $[m_j]$; viz the n_1 first days are transient, the m_1 following days are persistent, the n_2 following days are transient, etc. Then, the *random definition* consists in performing two random permutations s and s' of the n_j's and the m_j's and in defining the new persistent dataset as the one which arises from the new ordering of the $n_{s(j)}$'s and $m_{s'(j)}$'s. Repeating the above operations 100 times provides 100 estimates of persistence probability which are sorted into ascending order. The interval between the 5th and the 95th then constitute the 90% confidence interval for the null hypothesis. Consequently, when the estimated probability falls above (below) the confidence interval, we may state with 5% chance of being wrong that anomalies are generally persistent (transient).

To each curve and to each longitude in Fig. 16 corresponds a confidence interval, but we found that this interval does not fluctuate a lot in longitude and depends weakly on the considered data. For the sake of simplicity, we thus display a unique regular band for the confidence interval.

APPENDIX C

The Doom of the Correlation Criterion

We briefly present the persistence probability for the red noise when computed using a correlation criterion. The criterion is defined like in Horel (1985) and Mo (1986), using spatial correlations between large-scale anomalies over the whole channel. Five-day sequences are inspected: if during a sequence the correlation between all the couples of anomalies exceeds 0.8, the 5 days of the sequence are retained as persistent days. For red noise the persistent dataset contains 17 599 days out of 45 000.

Figure C1 shows the corresponding persistence probability computed as in section 5c. As mentioned in section 5a, the correlation criterion clearly selects high amplitude anomalies, whatever the shape. Only 10% of the anomalies are retained near the mean flow while more than 80% are retained in some places near the boundaries, and figures are very significant. Since these anomalies tend to concentrate on the x_1 axis, a strong bimodability occurs in the x_1-direction on the x_1–x_2 histogram (not shown).

As explained by Mo and Ghil (1987), pattern correlations can be interpreted in a geometric way as measures of the angle between phase space vectors associated with the patterns. For the red noise model defined by Eq. 4.10 and if the anomaly $Y_n - \bar{X}$ is small, Y_{n+1} is mainly defined by the random process W_n. Then the angle between successive vectors varies also at random, while when the anomaly $Y_n - \bar{X}$ is larger

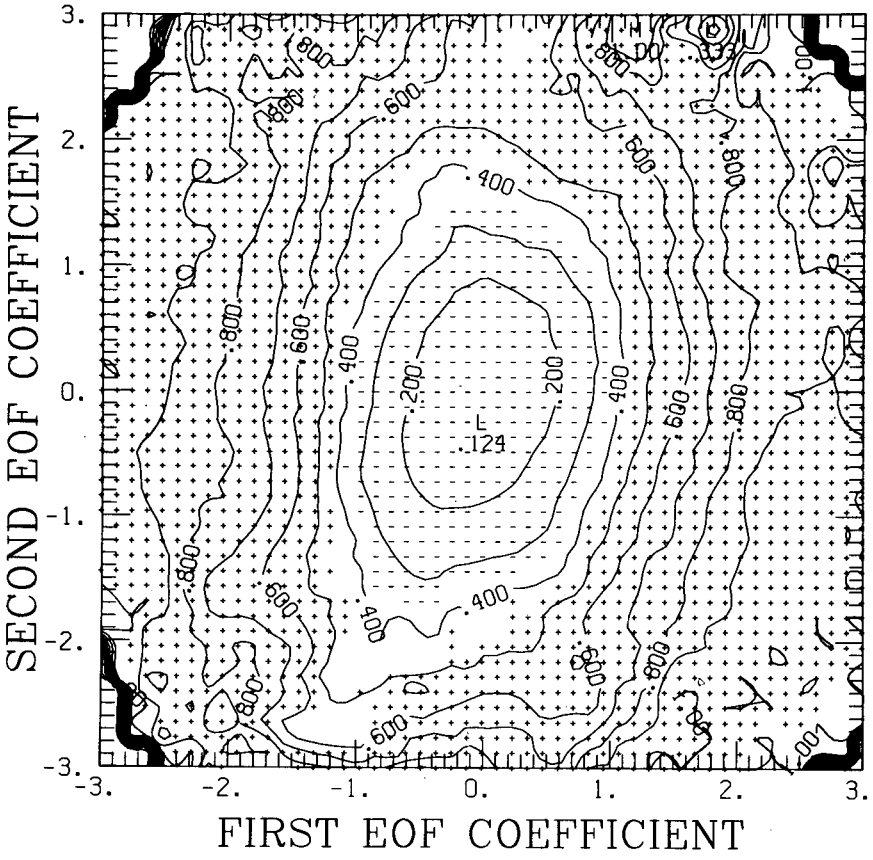

FIG. C1. As in Fig. 19 except for the correlation criterion.

than the standard deviation of W_n, the angle is determined by the linear regression. Depending on the ratio between the standard deviations of W_n and $Y_n - \bar{X}$, the criterion may spuriously reject low amplitude anomalies. The bimodality found for the red noise model shows clearly that this ratio is large enough. However, recall that we are considering data with a small number of degrees of freedom (seven large-scale modes), and that the spurious effects of correlation criterion may be reduced with more numerous degrees of freedom, since the proximity to the average flow is then less probable.

REFERENCES

Barnett, T. P., 1983: Interaction of the Monsoon and Pacific trade wind system at interannual time scales. Part I: the equatorial zone. *Mon. Wea. Rev.*, **111,** 756–773.

Berry, F. A., E. Bollay and N. R. Beers, 1973: *Handbook of meteorology.* McGraw-Hill.

Blackmon, M. L., 1976: A climatological spectral study of the 500 mb geopotential height of the Northern Hemisphere. *J. Atmos. Sci.*, **33,** 1607–1623.

——, J. M. Wallace, N.-C. Lau and S. L. Mullen, 1977: An observational study of the Northern Hemisphere wintertime circulation. *J. Atmos. Sci.*, **33,** 1040–1053.

Dole, R. M., 1985: Persistent anomalies of the extratropical Northern Hemisphere wintertime circulation: structure. *Mon. Wea. Rev.*, **114,** 178–207.

——, and N. D. Gordon, 1983: Persistent anomalies of the extratropical Northern Hemisphere wintertime circulation: geographical distribution and regional persistent characteristics. *Mon. Wea. Rev.*, **111,** 1567–1586.

Egger, J., and H.-D. Schilling, 1983: On the theory of the long-term variability of the atmosphere. *J. Atmos. Sci.*, **40,** 1073–1085.

Fraedrich, K., and H. Bottger, 1978: A wavenumber-frequency-analysis of the 500 mb geopotential at 50°N. *J. Atmos. Sci.*, **25,** 984–1002.

Frederiksen, J. S., 1982: A unified three-dimensional instability theory of the onset of blocking and cyclogenesis. *J. Atmos. Sci.*, **39,** 969–982.

Gutzler, D. S., and K. Mo, 1983: Autocorrelation of Northern Hemisphere geopotential heights. *Mon. Wea. Rev.*, **111,** 155–164.

——, and J. Shukla, 1984: Analogs in the wintertime 500 mb height field. *J. Atmos. Sci.*, **41,** 177–189.

Hansen, A. R., and A. Sutera, 1986: On the probability density distribution of planetary-scale atmospheric wave amplitude. *J. Atmos. Sci.*, **43,** 3250–3265.

Hayashi, Y., 1971: A generalized method of resolving disturbances into progressive and retrogressive waves by space Fourier and time cross-spectral analysis. *J. Meteor. Soc. Japan,* **49,** 125–128.

Held, I. M., 1983: Stationary and quasi-stationary eddies in the extratropical troposphere: Theory. *Large-Scale Dynamical Processes in the Atmosphere.* Academic Press. B. J. Hoskins and R. P. Pearce, Eds., pp. 127–168.

Holopainen, E., and C. Fortelius, 1987: High-frequency transient eddies and blocking. *J. Atmos. Sci.*, **44,** 1632–1645.

Horel, J. D., 1984: Complex principal components analysis: theory and examples. *J. C. Appl. Meteor.*, **23,** 1660–1673.

——, 1985: The persistence of the 500 mb height field during Northern Hemisphere winter. *Mon. Wea. Rev.*, **113,** 2030–2042.

Hoskins, B. J., I. N. James and G. H. White, 1983: The shape, propagation and mean-flow interaction of large-scale weather systems. *J. Atmos. Sci.*, **40,** 1595–1612.

Illari, L., and J. C. Marshall, 1983: On the interpretation of eddy fluxes during a blocking episode. *J. Atmos. Sci.*, **40,** 2232–2242.

Legras, B., and M. Ghil, 1985: Persistent anomalies, blocking and variations in atmospheric predictability. *J. Atmos. Sci.*, **42,** 433–471.

Lorenz, E. N., 1956: Empirical orthogonal functions and statistical weather prediction. *Scientific Report No 1,* Dept. of Meteorology, Massachusetts Institute of Technology, Cambridge, Massachusetts.

Mo, K. C., 1986: Quasi-stationary states in the Southern Hemisphere. *Mon. Wea. Rev.*, **114,** 808–823.

——, and M. Ghil, 1987: Statistics and dynamics of persistent anomalies. *J. Atmos. Sci.*, **44,** 877–901.

Mullen, S. L., 1987: Transient eddy forcing of blocking flows. *J. Atmos. Sci.*, **44,** 3–22.

Oort, A., 1983: Global atmospheric circulation statistics, 1958–1973. NOAA Prof. Paper No. 14, U.S. Govt. Printing Office, Washington, DC, 180 pp.

Pedlosky, J., 1979: Geophysical fluid dynamics. Springer-Verlag.

Pierrehumbert, R. T., 1984: Local and global instability of zonally varying flow. *J. Atmos. Sci.*, **41,** 2141–2162.

——, 1986: The effect of local baroclinic instability on zonal inhomogeneities of vorticity and temperature, *Advances in Geophysics,* **44,** B. Saltzman and R. Benzi, Eds.

Pratt, R. W., 1976: The interpretation of space time spectral quantities. *J. Atmos. Sci.*, **33,** 1060–1066.

Shutts, G. J., 1983: The propagation of eddies in diffluent jetstreams: eddy vorticity forcing of blocking flow fields. *Quart. J. R. Met. Soc.*, **109,** 737–761.

Simmons, A. J., and B. J. Hoskins, 1978: The life cycles of some nonlinear baroclinic waves. *J. Atmos. Sci.*, **35,** 414–432.

Thomas, J. B., 1969: An introduction to statistical communication theory. Wiley, 663 pp.

Trenberth, K. E., 1986: An assessment of the impact of transient eddies on the zonal flow during a blocking episode using localized Eliassen–Palm flux diagnostics. *J. Atmos. Sci.*, **43,** 2070–2087.

Vallis, G. K., 1985: On the spectral integration of the quasi-geostrophic equations for doubly-periodic and channel flow. *J. Atmos. Sci.*, **42,** 95–99.

Vautard, R., 1987: Les échelles de temps de la circulation atmosphérique: couplage interne et approches de la paramétrisation des modes rapides, thèse de Doctorat, Université Pierre et Marie Curie, Paris (in english).

——, and B. Legras, 1988: On the source of midlatitude low-frequency variability. Part II: Nonlinear equilibration of weather regimes. *J. Atmos. Sci.*, **415,** 2845–2867.